Isolation of a bent dysprosium bis(amide) single-molecule magnet

Jack Emerson-King,[1] Gemma K. Gransbury,[1] George F. S. Whitehead,[1] Iñigo J. Vitorica-Yrezabal,[1] Mathieu Rouzières,[2] Rodolphe Clérac,[2,*] Nicholas F. Chilton,[1,3]* and David P. Mills[1,*]

[1]*Department of Chemistry, The University of Manchester, Oxford Road, Manchester, M13 9PL, UK.*

[2]*Univ. Bordeaux, CNRS, CRPP, UMR 5031, 33600 Pessac, France.*

[3]*Research School of Chemistry, The Australian National University, Sullivans Creek Road, Canberra, ACT, 2601, Australia.*

**Email:* rodolphe.clerac@u-bordeaux.fr; nicholas.chilton@manchester.ac.uk; david.mills@manchester.ac.uk

Abstract

The isolation of formally two-coordinate lanthanide (Ln) complexes is synthetically challenging, due to predominantly ionic Ln bonding regimes favoring high coordination numbers. In 2014 some of us predicted that a near-linear dysprosium bis(amide) cation $[Dy\{N(Si^iPr_3)_2\}_2]^+$ could provide a single-molecule magnet (SMM) with an energy barrier to magnetic reversal (U_{eff}) of up to 2600 K, a threefold increase of the record U_{eff} for a Dy SMM at the time; this work showed a potential route to SMMs that can provide high-density data storage at higher temperatures. However, synthetic routes to a Dy complex containing only two monodentate ligands have not previously been realized. Here we report the synthesis of the target bent dysprosium bis(amide) complex, $[Dy\{N(Si^iPr_3)_2\}_2][Al\{OC(CF_3)_3\}_4]$ (**1-Dy**), together with the diamagnetic yttrium analog. We find U_{eff} = 924(17) K for **1-Dy**, which is much lower than the predicted values for idealized linear two-coordinate Dy(III) cations. *Ab initio* calculations of the static electronic structure disagree with the experimentally-determined height of the U_{eff} barrier, thus magnetic relaxation is faster than expected based on magnetic anisotropy alone. We propose that this is due to enhanced spin-phonon coupling arising from the flexibility of the Dy coordination sphere, in accord with ligand vibrations being of equal importance to magnetic anisotropy in the design of high-temperature SMMs.

Introduction

Raising the temperatures at which single-molecule magnets (SMMs) exhibit magnetic remanence is key to unlocking their potential applications in high-density data storage, as the liquid helium cooling currently required is expensive.[1–3] For the last two decades lanthanide (Ln) SMMs have shown the most promise to achieve this goal,[4–7] with axial dysprosium complexes predicted to show the highest energy barriers to magnetic reversal (U_{eff}).[8–10] As the isolation of an ideal axial two-coordinate linear Dy(III) complex is a major synthetic challenge, pentagonal bipyramidal Dy complexes with strongly donating apical alkoxides and five weak equatorial donor ligands were the first SMMs to achieve U_{eff} values > 1000 K.[11] Salts with axial dysprosocenium cations $[Dy(Cp^R)_2]^+$ (Cp^R = substituted cyclopentadienyl) and related derivatives subsequently raised 100 s magnetic blocking temperatures (T_B) ever-closer to the boiling point of liquid nitrogen (77 K);[12–22] this was attributed to the rigidity of the coordinated aromatic ligands hindering Raman magnetic relaxation pathways.[12,23] The current record-holding SMM $[Dy_2(C_5{}^iPr_5)_2(\mu\text{-}I)_3]$ contains a $1e^-$ Dy–Dy bond, and has U_{eff} = 2345(36) K and T_B = 72 K.[19]

Prior to the isolation of these high-barrier SMMs, some of us reported the syntheses of the near-linear Ln complexes $[Ln\{N(Si^iPr_3)_2\}_2]$ (Ln = Sm, Eu, Tm, Yb).[24,25] We used the experimentally-determined atomic coordinates of the Sm(II) derivative (N–Ln–N: 175.5(2)°) to calculate that an analogous Dy(III) bis(amide) cation $[Dy\{N(Si^iPr_3)_2\}_2]^+$ could show $U_{eff} \approx 2600$ K;[24] this value was over triple the magnitude of the record barrier for Dy SMMs at the time (842 K for a polymetallic Dy-doped yttrium alkoxide complex).[26] Further calculations revealed that U_{eff} values could remain > 1300 K even if the N–Dy–N angle was reduced to as low as 120°, provided that no additional ligands coordinated.[27] In the interim, we synthesized the bent Ln(III) bis(amide) complexes $[Ln\{N(Si^iPr_3)_2\}_2][B(C_6F_5)_4]$ for Ln = Sm, Tm and Yb, using the parent Ln(II) complexes $[Ln\{N(Si^iPr_3)_2\}_2]$ as starting materials;[24,25,28,29] recently, a related bent Yb(III) bis(amide) complex, $[Yb\{N(SiPh_2Me)_2\}_2][Al\{OC(CF_3)_3\}_4]$, has been reported.[30] However, due to synthetic difficulties associated with installing bulky silylamides at small, charge-dense Ln(III) centers, we had previously been unable to access the desired Dy(III) bis(amide) cation $[Dy\{N(Si^iPr_3)_2\}_2]^+$. Indeed, the isolation of any Dy complex containing only two monodentate ligands has proved elusive for the wider

synthetic chemistry community to date, which is particularly hampered by the predominantly ionic bonding regimes of relatively large Ln cations favoring higher coordination numbers (CNs).[31–33]

Here we report the isolation and characterization of the bent Dy bis(amide) complex $[Dy\{N(Si^iPr_3)_2\}_2][Al\{OC(CF_3)_3\}_4]$ (**1-Dy**), together with the diamagnetic yttrium analog **1-Y**, and other complexes that were prepared as starting materials to these synthetic targets. Magnetic measurements reveal that the SMM properties of **1-Dy** are not as advantageous as originally predicted. *Ab initio* calculations show that the bent geometry still imposes very large magnetic anisotropy in **1-Dy**, as large as for the first dysprosocenium cation $[Dy(Cp^{ttt})_2]^+$.[12,15,16] As molecular rigidity has been shown to be crucial for controlling spin-phonon relaxation in dysprosocenium cations,[12] we propose that the flexible coordination environment in **1-Dy** enables rapid magnetic relaxation; the large magnetic anisotropy generated by crystal field (CF) splitting will therefore not necessarily result in a high-barrier Ln SMM unless spin-phonon relaxation enabled by molecular vibrations is adequately controlled.

Results

Synthesis. Complexes **1-Ln** were prepared by the stepwise synthetic route shown in Scheme 1. Analysis of mass balances indicated that all reactions proceed with essentially quantitative conversions, and this was in accord with *in situ* ^{1}H NMR spectra for the Y congeners. The separate salt elimination reactions of $[Ln(BH_4)_3(THF)_3]$ (Ln = Y, Dy)[34] with one equivalent of $[K\{N(Si^iPr_3)_2\}]$[24] in fluorobenzene at ambient temperature for 1 h gave the heteroleptic Ln(III) mono(amide) bis(borohydride) complexes $[Ln\{N(Si^iPr_3)_2\}(BH_4)_2(THF)]$ (**2-Ln**) in 79-83% isolated yields following filtration and crystallization from *n*-hexane at –35 °C. The bound THF was removed from **2-Ln** by heating solid samples at 120 °C for 2 h at 0.01 mbar. Recrystallization of the desolvated product from 1,2-difluorobenzene layered with *n*-hexane gave, by slow diffusion, crystals of the tetranuclear Ln(III) complexes $[Ln\{N(Si^iPr_3)_2\}(BH_4)(\mu\text{-}BH_4)]_4$ (**3-Ln**) in 54-67% isolated yields. It is critical to remove all of the KBH_4 evolved during the synthesis of **2-Ln**; failure to do so has a deleterious impact on the thermal desolvation step. Additionally we found that samples of **3-Ln** recrystallized in the presence of trace amounts of KBH_4 were contaminated with several

crystals of the adducts $[\{Ln\{N(Si^iPr_3)_2\}(BH_4)(\mu\text{-}BH_4)\}_2\{K(\mu\text{-}BH_4)\}]_\infty$ (**3-Ln·0.5KBH$_4$**), for which we include the single crystal XRD structures for completeness. The experimental procedures described herein provide pure samples of **2-Ln**.

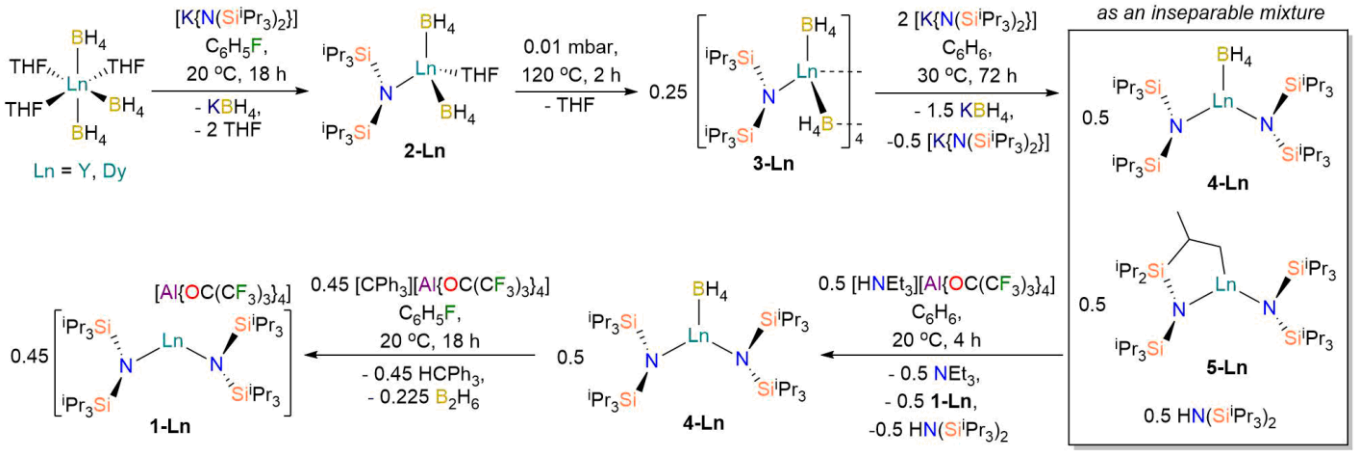

Scheme 1. Synthesis of **1-Ln**, **2-Ln**, **3-Ln**, **4-Ln** and **5-Ln** (Ln = Y, Dy).

The separate salt elimination reactions of **3-Ln** with an excess (2 eq.) of $[K\{N(Si^iPr_3)_2\}]$ in benzene at the optimal temperature of 30 °C for 72 h gave full conversion to a mixture of the desired Ln(III) bis(amide) borohydride complexes $[Ln\{N(Si^iPr_3)_2\}_2(BH_4)]$ (**4-Ln**), species assigned as the Ln(III) cyclometalates $[Ln\{N(Si^iPr_3)_2\}\{N(Si^iPr_3)[Si(^iPr)_2\{CH(Me)CH_2\}]\text{-}\kappa^2\text{-}N,C\}]$ (**5-Ln**), and $HN(Si^iPr_3)_2$; this product distribution is in accord with deprotonation of a silyl group *in situ*. The physical separation of these three highly alkane-soluble species proved challenging; as such the mixture was treated with 0.5 eq. of $[HNEt_3][Al\{OC(CF_3)_3\}_4]$[28] in benzene at 20 °C for 30 min, in order to protonate **5-Ln** and generate the target homoleptic Ln(III) bis(amide) complexes **1-Ln**. After removal of benzene and NEt_3 under vacuum, the oily solid was triturated with *n*-hexane to give a mixture of **4-Ln**, $HN(Si^iPr_3)_2$ and solid **1-Ln**. Filtration and recrystallization of **4-Ln** from hexamethyldisiloxane at –30 °C enabled its separation from $HN(Si^iPr_3)_2$. Unfortunately, fluorobenzene solutions of the hydrocarbon-insoluble components layered with *n*-hexane consistently gave crystals of **1-Ln** contaminated with $[HNEt_3][Al\{OC(CF_3)_3\}_4]$, even when the ammonium salt was used sub-stoichiometrically. As such, pure samples of **1-Ln** were prepared in 73-79% crystalline

yields by a hydride abstraction strategy *via* the reaction of isolated **4-Ln** with 0.9 eq. of $[CPh_3][Al\{OC(CF_3)_3\}_4]$[35] in fluorobenzene at 20 °C for 18 h, followed by slow diffusion of *n*-hexane into the resulting solutions. Treating a mixture of **1-Y** and $[HNEt_3][Al\{OC(CF_3)_3\}_4]$ with excess $[K\{N(Si^iPr_3)_2\}]$ gives ^{1}H, $^{13}C\{^1H\}$ DEPTQ, $^{29}Si\{^1H\}$ DEPT90, and ^{19}F NMR spectra that are consistent with the concomitant formation of **5-Y**, $HN(Si^iPr_3)_2$ and $K[Al\{OC(CF_3)_3\}_4]$. We have not yet been able to isolate **5-Ln** in pure form for further characterization, but NMR data for a C_6D_6 solution of a 1:2 mixture of **5-Y** and $HN(Si^iPr_3)_2$ are in line with the proposed cyclometalate formulation (see below).

Spectroscopic characterization. Bulk samples of crystalline **1-Ln**, **2-Ln**, **3-Ln** and **4-Ln** were characterized by elemental analysis, multinuclear NMR and ATR-IR spectroscopies (see Supporting Information Figures S1–S48 for annotated NMR spectra of **1-Ln**, **2-Ln**, **3-Ln**, **4-Ln** and **5-Y**). The ^{1}H and $^{13}C\{^1H\}$ DEPTQ NMR spectra of **1-Y** in C_6H_5F solution show the anticipated resonances for the methyl and methine environments of the ^{i}Pr groups, with no additional Y-C or Y-H coupling observed (^{89}Y, I = ½, 100% abundant). The $^{29}Si\{^1H\}$ DEPT90 NMR spectrum of **1-Y** shows a single resonance at δ_{Si} = –4.8 ppm, while no resonance was observed in the corresponding spectrum of **1-Dy**. The ^{19}F NMR spectrum of the $[Al\{OC(CF_3)_3\}_4]^-$ anion of **1-Dy** contains a single broad resonance at δ_F = –97.2 ppm (full width half maximum, fwhm ≈ 280 Hz), that is paramagnetically shifted relative to that seen for **1-Y** (δ_F = –75.1 ppm).

The ^{1}H, ^{11}B, $^{13}C\{^1H\}$ DEPTQ, and $^{29}Si\{^1H\}$ DEPT90 NMR spectra of diamagnetic **2-Y**, **3-Y** and **4-Y** were fully assigned in C_6D_6 solution. For brevity we do not provide a full discussion of all resonances in the ^{1}H and $^{13}C\{^1H\}$ DEPTQ NMR spectra here as chemical shifts and coupling constants were in line with expected values for the functional groups present. In C_6D_6, the ^{11}B NMR spectra of **2-Y** and **4-Y** feature a single pentet resonance at δ_B = –22.0 ppm ($^1J_{BH}$ = 81 Hz) and δ_B = –21.4 ppm ($^1J_{BH}$ = 86 Hz), respectively. By contrast for **3-Y** two broad resonances are observed at δ_B = –20.7 and –3.6 ppm, which we assign as the terminal and bridging BH_4 groups, respectively, implying that this species remains oligomeric in benzene solution. In 1,2-difluorobenzene, a broad pentet resonance is observed at δ_B = –20.9 ppm ($^1J_{BH}$ = 80 Hz) for **3-Y**, consistent with a fluxional monomeric species, possessing equivalent time-averaged

terminal BH_4 groups. The $^{29}Si\{^1H\}$ DEPT90 NMR spectra of **2-Y**, **3-Y** and **4-Y** in C_6D_6 each contain a similarly shielded singlet resonance; (δ_{Si}/ppm = –2.7, **2-Y**; –3.7, **3-Y**; –3.4, **4-Y**); with **3-Y** no significant difference is observed in 1,2-difluorobenzene (δ_{Si} = –3.6 ppm), Interpretation of the NMR data for **2-Dy**, **3-Dy** and **4-Dy** was limited due to paramagnetic broadening of signals, though the $^{11}B\{^1H\}$ NMR spectra each contain a single resonance (δ_B/ppm = –18.1, **2-Dy**; –9.9, **3-Dy**; –14.1, **4-Dy**). Additionally, the solution magnetic susceptibilities of these complexes were determined at 298 K by the Evans method;[36] all values obtained (range χT = 12.5–14.2 cm^3 K mol^{-1}) are in line with that expected for a Dy(III) free ion (χT = 14.17 cm^3 K mol^{-1}).[37]

The species assigned as the cyclometalate **5-Y** exhibits three signals in the $^{29}Si\{^1H\}$ DEPT90 NMR spectrum at –3.2, –5.8 and –7.6 ppm. Three magnetically inequivalent silyl groups are also seen in the corresponding ^1H and $^{13}C\{^1H\}$ DEPTQ NMR spectra; the latter spectrum contains a doublet resonance at δ_C = 55.3 ppm; $^1J_{YC}$ = 47.4 Hz with the correct phase for a methylene group, which was assigned to the Y-bound carbon atom. Due to the presence of multiple coincident resonances in ^1H-^{13}C HSQC and ^1H-^{13}C HMBC NMR spectra we were unable to assign the associated ^1H resonances, precluding a definitive assignment of molecular connectivity. The resonances assigned to **5-Y** in the ^1H, $^{13}C\{^1H\}$ DEPTQ and $^{29}Si\{^1H\}$ DEPT90 NMR spectra of **5-Y** are comparable to the those previously reported for the Y(III) silylamide cyclometalate [Y{N(SiMe$_3$)$_2$}$_2${N(SiMe$_3$)[Si(Me)$_2$CH$_2$]-κ^2-*N*,*C*}K], which has δ_{Si} = –26.1, –13.5 and –12.0 ppm, and also shows resonances for the bound methylene group at δ_H = –1.27 ppm ($^2J_{YH}$ = 2.6 Hz) and δ_C = 23.6 ppm ($^1J_{YC}$ = 22.9 Hz).[38]

The ATR-IR spectra of each Dy/Y pair in **1-Ln**, **2-Ln**, **3-Ln** and **4-Ln** overlap with each other, and show a number of red-shifted C–H stretching bands that are diagnostic of some methine and methyl groups being in close proximity to the Ln centers (see Supporting Information Figures S49–S56). These spectroscopic markers were corroborated by density-functional theory (DFT)-calculated IR spectra for **1-Y**, **2-Y**, **3-Y** and **4-Y** (see Supporting Information Figures S57–S60), and are in accord with their crystallographically-determined solid-state structures (see below and Supporting Information Figures S61–S70). For **1-Ln** these features extend down to 2560 cm^{-1}, with the lowest energy modes computationally

assigned to the methine C–H group that is closest to the Ln center; the corresponding resonance for **3-Ln** is at 2745 cm^{-1}, and for **4-Ln** there are two bands at 2756 cm^{-1} and 2729 cm^{-1}. Characteristic borohydride vibrations were also observed for **2-Ln**, **3-Ln** and **4-Ln**;[39] the apical B–H stretch of the terminal borohydrides correspond to sharp features at 2486 cm^{-1}, 2519 cm^{-1}, and 2495 cm^{-1} for **2-Ln**, **3-Ln** and **4-Ln** respectively, whilst the stretching modes of the B–H bonds that are proximal to the metal give broad, convoluted bands between 2360 and 2060 cm^{-1} for all complexes.

Solid-state structural characterization. The solid-state structures of **1-Ln**, **2-Ln**, **3-Ln** and **4-Ln** and **3-Ln·0.5KBH$_4$** were characterized by single crystal X-ray diffraction (XRD); all bond distances and angles are in line with expected values and these only vary to a small extent for each Dy/Y pair in accord with the difference in six-coordinate ionic radii of Dy(III) (0.912 Å) and Y(III) (0.900 Å),[40] thus we focus our discussion herein on the target axial Dy(III) bis(amide) cation in **1-Dy** (Figure 1). The remaining structures and all crystallographic parameters are collated in the Supporting Information (see Figures S61–S70 and Tables S1–S3).

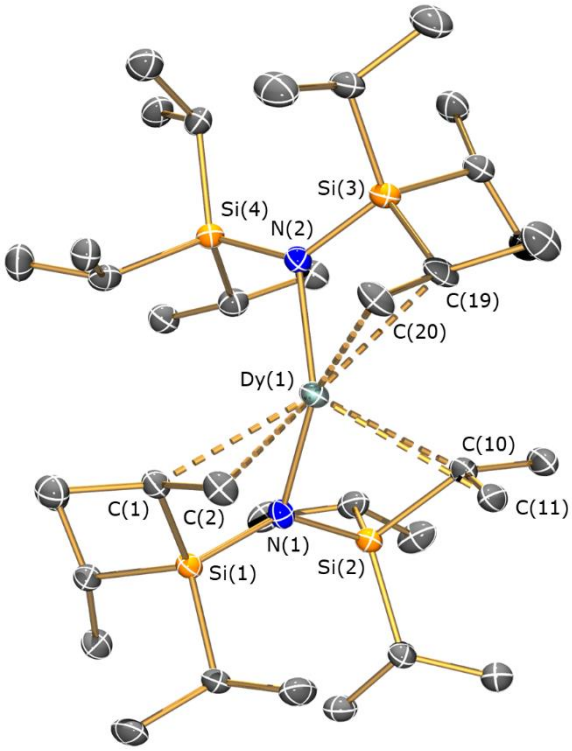

Figure 1. Solid-state structure of the cation of **1-Dy** at 100(2) K. Displacement ellipsoids set at 50% probability level. Hydrogen atoms and $[Al\{OC(CF_3)_3\}_4]^-$ counter-anion omitted for clarity. Selected bond distances (Å) and angles (°): Dy(1)–N(1): 2.209(5); Dy(1)–N(2): 2.202(5); Dy(1)···C(1): 2.845(5); Dy(1)···C(2): 2.987(6); Dy(1)···C(10): 2.883(7); Dy(1)···C(11): 3.036(7); Dy(1)···C(19): 2.863(6); Dy(1)···C(20): 2.929(6); Dy(1)···Si(1): 3.215(2); Dy(1)···Si(2): 3.229(2); Dy(1)···Si(3): 3.207(2); N(1)–Dy(1)–N(2): 128.7(2).

The $[Dy\{N(Si^iPr_3)_2\}_2]^+$ cation exhibits a bent geometry, with a N–Dy–N angle that deviates significantly from linearity (128.7(2)°), with the NSi_2 fragments in a staggered conformation (twist angle: 63.12(6)°), and mean Dy–N distances of 2.206(7) Å. The structure of this cation is similar to the previously reported Sm, Tm and Yb congeners,[28] with deviations in metrical parameters expected on the basis of variation of Ln(III) cation size and Lewis acidity.[31] In common with the previously reported heavy $[Ln\{N(Si^iPr_3)_2\}_2]^+$ cations, the Dy coordination sphere of **1-Dy** is completed by three short Dy···Si (range: 3.207(2)–3.229(2) Å), six short Dy···C (range: 2.845(5)–3.036(7) Å), and six short Dy···H distances (range: 2.293–2.455 Å) to methine and methyl fragments of three different ^{i}Pr groups. These interactions are presumably driven by the electrostatic stabilization of the coordinatively unsaturated Dy(III) center by the electron density of the Si–C/C–H bonds of the silyl groups, as previously described for Sm, Tm and Yb congeners.[28] Powder XRD was performed on a sample of microcrystalline **1-Dy** (see Supporting Information Figure S71 and Table S4), confirming that the single crystal structure obtained is representative of the bulk crystalline material used for magnetic characterization.

Magnetic measurements. The static and dynamic magnetic properties of **1-Dy** in the solid-state and as a 200 mM frozen solution sample in fluorobenzene were probed by dc (direct current) and ac (alternating current) susceptibility measurements (see Supporting Information Figures S72–S98 and Tables S5–S9). The χT value determined at 300 K under a 0.1 T dc field (14.75 cm^3 K mol^{-1}, Figure S72) is slightly higher than that determined at 298 K in fluorobenzene solution (12.97 cm^3 K mol^{-1}, Figure S73) and the expected

Dy(III) free ion value (14.17 cm^3 K mol^{-1}).[37] We observe a regular decrease in χT with decreasing temperature as excited CF states are thermally depopulated until *ca*. 10 K where there is a sharper decrease, reaching χT = 7.71 cm^3 K mol^{-1} at 2 K (Figure S72); zero field-cooled (ZFC) and field-cooled (FC) data collected in a smaller 0.001 T or 0.005 T dc field show that this drop is mainly due to Zeeman depopulation effects, dropping only to χT = 11.3 cm^3 K mol^{-1} at 1.85 K (Figures S75 and S76). Magnetization *vs.* field experiments show that the magnetization saturates at M_{sat} = 5.42 μ_B under a 7 T applied dc field (Figure S77), suggesting an m_J = ±15/2 ground state (M_{sat} = 5.00 μ_B).[7] Rapid quantum tunneling of magnetization (QTM) at zero field is also evident from the *M vs. H* hysteresis loops (Figure 2), where **1-Dy** shows a waist-restricted loop that is typical for Ln SMMs,[5] and is closed at zero field at 2 K (Figure S79).

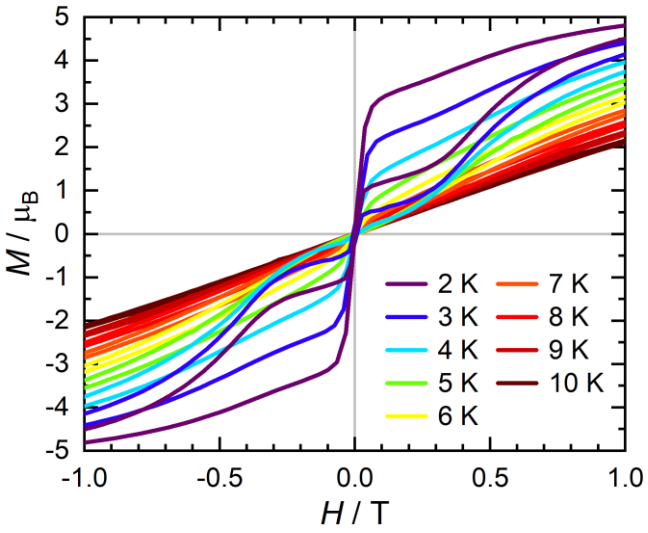

Figure 2. *M vs. H* hysteresis loops of **1-Dy** suspended in eicosane from 2–10 K in between –1 T to +1 T. Sweep rate is 22 Oe s^{-1}.

Ac susceptibility measurements of polycrystalline **1-Dy** were performed up to 10 kHz to study the slow magnetic relaxation. Temperature- and frequency-dependent behavior were seen for the in-phase (χ') and out-of-phase (χ'') components of ac susceptibility in zero dc field, with maxima in χ'' due to slow relaxation of the magnetization present between 2 and 110 K (Figures S87 and S88, Table S5).[41] The ac data were fit using the generalized Debye model[41,42] to extract relaxation rates along with estimated

standard deviations (ESDs)[43,44] as a function of temperature. The temperature-dependence of the magnetic relaxation rates suggest Orbach relaxation at high temperatures, Raman-I relaxation at intermediate temperatures, and QTM at the lowest temperatures (Figure 3).[2] The temperature-dependent relaxation rates corresponding to these processes were modelled using Eqn 1 in CC-FIT2 5.6.4,[43,45] giving: U_{eff} = 945(24) K, $\tau_0 = 10^{-8.53(9)}$ s, $C = 10^{-4.0(2)}$ s^{-1} K^{-n}, n = 3.9(1), $\tau_{QTM} = 10^{-1.00(5)}$ s (Figure S97); note that T_B is not defined as τ < 100 s at all temperatures.

$$\tau^{-1}(\mathrm{T}) = CT^n + \tau_0^{-1}\exp\left(-\frac{U_{\text{eff}}}{T}\right) + \tau_{QTM}^{-1} \qquad \text{(Eqn 1)}$$

$$\tau^{-1}(\mathrm{H}) = \frac{\tau_{QTM}^{-1}}{1+QH^p} + C_{\mathrm{T}} + DH^m \qquad \text{(Eqn 2)}$$

$$\tau^{-1}(\mathrm{H,T}) = \frac{\tau_{QTM}^{-1}}{1+QH^p} + CT^n + AH^m T + \tau_0^{-1}\exp\left(-\frac{U_{\text{eff}}}{T}\right) \qquad \text{(Eqn 3)}$$

Additional temperature-dependent ac susceptibility measurements in a 0.08 T dc field (Figures S89, S90 and S99, Table S6) indicate that QTM is quenched in this field. Performing an ac susceptibility experiment at 12 K as a function of magnetic field allows us to investigate field-dependent relaxation dynamics (Figures S91 and S92, Table S7). The relaxation rate decreases with increasing field below *ca*. 400 Oe, then plateaus until *ca*. 4000 Oe, above which it increases again (Figure 4). This is consistent with quenching of QTM in low fields,[46,47] followed by a plateau defined by the field-independent processes (predominately the Raman-I mechanism[48] as the Orbach contribution is insignificant at 12 K), and then an increase at higher fields owing to either a field-dependent Raman-II or Direct single-phonon mechanism.[47,48] Fitting these data with a model accounting for these three terms (Eqn 2) gives: $\tau_{QTM} = 10^{-1.01(1)}$ s, $Q = 10^{-7.7(3)}$ Oe^{-p}, p = 3.7(1), $C_{12\,\mathrm{K}} = 10^{0.103(3)}$ s^{-1}, $D = 10^{-14.2(3)}$ s^{-1} Oe^{-m}, m = 3.72(8) (Figure S98). The zero-field QTM timescale (τ_{QTM}) is in excellent agreement with that obtained from the zero-field ac data, and the field exponent (p) agrees well with that found for the axial SMM [Dy(O^{t}Bu)(Cl)(THF)$_5$][B(C$_6$F$_5$)$_4$] of 3.8(2).[46] The field-independent Raman-I rate is $C_{12\,\mathrm{K}} = 10^{0.103(3)} \sim 1.27$ s^{-1} which corresponds well to the expected 12 K Raman-I rate obtained from the zero-field (~1.69 s^{-1}) or the 0.08 T (~1.07 s^{-1}) parameters. Finally, the field exponent of the Raman-II/Direct term m = 3.72(8) is

approaching the value expected for the single-phonon Direct process in the high-temperature limit of m = 4,[49] and so we suggest this is a more-likely mechanism; however, we cannot rule out a contribution from the Raman-II mechanism.

We resolved to find a set of global parameters to describe the relaxation processes in **1-Dy** by simultaneous fitting of the three datasets to Eqn 3. As the high-field process is only observable in the 12 K dataset, we do not have sufficient information to determine the temperature depdencence of this process (which would be expected to have a linear or power-law T-dependence for the Direct or Raman-II relaxation processes, respectively[48,50]), and so we simply assume a linear temperature dependence. We used values from the individual fits as starting parameters, and performed the first optimisation with Q and p fixed before allowing all parameters to freely refine. This gives global best-fit parameters: U_{eff} = 924(17) K, τ_0 = $10^{-8.45(7)}$ s, C = $10^{-4.31(5)}$ s^{-1} K^{-n}, n = 4.05(3), τ_{QTM} = $10^{-1.09(4)}$ s, Q = $10^{-14(17)}$ Oe^{-p}, p = 7(7), A = $10^{-15(4)}$ s^{-1} Oe^{-m} K^{-1}, m = 4(1) (Figures 3, 4 and S99). The field-independent QTM rate and the Orbach, Raman-I and Direct/Raman-II parameters are not significantly changed from the individual fits. However, the field-dependence of QTM process is increased and poorly defined (large errors in Q and p) relative to the 12 K parameters: this reflects the efficient quenching of QTM in the 0.08 T dataset, which exhibits a downturn in the temperature-dependent rates at the lowest temperatures (Figure S99). However, our model does not account for any possible non-power law temperature-dependence of Raman-I relaxation at low temperatures,[48] which could explain the downturn in rates, nor does it account for any possible temperature-dependence of QTM,[47] thus we believe the field-dependence of QTM to be overestimated by the global fit.

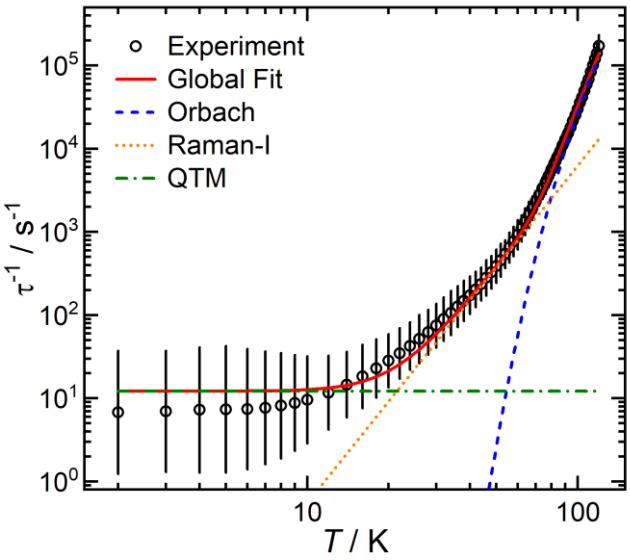

Figure 3. Temperature dependence of the magnetic relaxation rate (τ^{-1}) of **1-Dy** in zero dc field. Bars denote ESDs of distribution of rates from the generalized Debye model.[41,42]

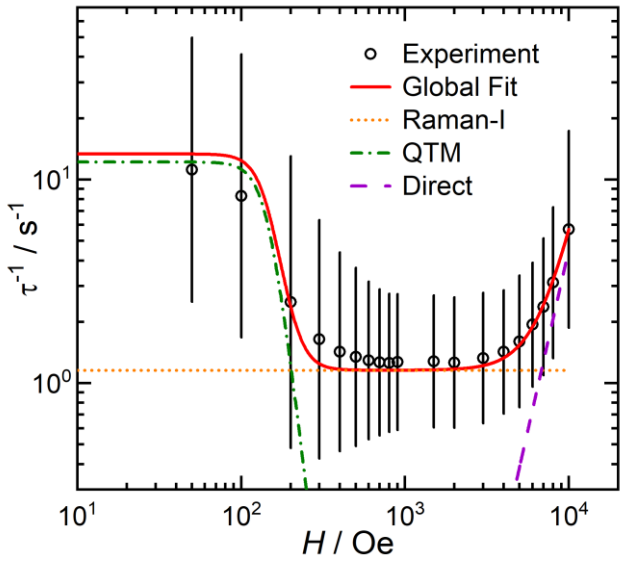

Figure 4. Field dependence of the magnetic relaxation rate (τ^{-1}) of **1-Dy** at 12 K. Bars denote ESDs of distribution of rates from the generalized Debye model.[41,42] Orbach contribution (10^{-26} s^{-1}) not shown.

Some of us have previously shown that linearity of the N–Dy–N angle in bis-amide complexes should correlate with U_{eff}.[27] We hypothesized that in solution the N–Dy–N angle in **1-Dy** may increase, as has been observed for the Yb congener.[28] A *ca*. 200 mM solution of **1-Dy** in fluorobenzene was prepared by dissolving a known mass of solid in the appropriate mass of solvent, and this solution was flash-frozen

in liquid nitrogen. Although we cannot completely discount the possibility that some precipitation occurs, we found that concentrated fluorobenzene solutions of **1-Dy** stored overnight at *ca*. 250 K do not readily crystallize in the absence of alkane anti-solvents, and the melting point of fluorobenzene (229 K) is relatively high. The ac susceptibility experiments for the frozen solution sample give relatively noisy data (Figure S93), but the Cole-Cole profiles are much broader and more asymmetric than the solid-state data and cannot be modelled well by the generalized Debye model. The low-temperature (2–13 K) data can be fit by a phenomenological Havriliak-Negami model (Figures S94 and S95, Table S8) that accounts for skew as well as a distribution in relaxation times.[51] At higher temperatures (31–79 K), a shoulder in the Cole-Cole plot emerges and the ac data are best fit by a double generalized Debye model (Figures S96 and S97 and Table S9). Furthermore, magnetic hysteresis loops are more open in frozen solution than in the solid state (but remain waist-restricted, Figures S84–S86). The low-temperature frozen solution relaxation data show a comparable QTM rate to the solid-state sample, whereas the high-temperature fits encompass a major component (65%) that has rates in line with the solid-state data, and a minor component (35%) that has considerably slower dynamics (Figure S100). Whilst some of these relaxation data could be explained by precipitation of **1-Dy**, the minor component and the hysteresis data are both in accord with a sample that relaxes measurably slower than the solid-state material. These observations are consistent with the frozen solution sample containing a broader and more asymmetric distribution of molecular geometries, with some molecules in the distribution having larger N–Dy–N angles and hence larger anisotropy and slower magnetic relaxation rates.

Ab initio calculations. First-principles complete active space self-consistent field spin-orbit (CASSCF-SO) calculations were performed using the atomic coordinates of the cation in **1-Dy** determined by single crystal XRD and OpenMolcas.[52] These calculations show that the ground state is an almost pure m_J = ±15/2 Kramers doublet, with Ising-like g-values ($g_x = g_y = 0$, $g_z = 19.86$; Table S10). The first two excited Kramers doublets are also strongly axial, lying 616 K (98% m_J ±13/2, 0.8° between excited g_z and ground g_z) and 1185 K (94% m_J ±11/2, 1.6°) above the ground state (Figure S99).[12]

Discussion

All previously reported examples of axial Dy SMMs with no equatorial donor ligands contain bulky η^5-cyclopentadienyl ligands or related derivatives,[12–22] hence there is no literature precedent for refined magnetostructural comparisons with **1-Dy**. The Dy(III) ion in **1-Dy** is bound by two monodentate σ-donor bis(silyl)amides; although some of the charge density is delocalized about the ligand scaffolds due to negative hyperconjugation with the triisopropylsilyl groups,[53,54] the N atoms can be formally treated as point charge Lewis bases to a first approximation. This differs from the highest-performing Dy SMMs bound by π-aromatic ligands in the literature,[12–22] which donate electron density to Dy from delocalized molecular orbitals located about a pentagonal arrangement of atoms. Accordingly, the degree of magnetic anisotropy and the purity of m_J states should be more sensitive to deviations from ideal linearity in complexes like **1-Dy** than for a sandwich-type complex. We previously reported the solid-state structures of the bent Tm(III) complex $[Tm\{N(Si^iPr_3)_2\}_2][B(C_6F_5)_4]$ (N–Tm–N: 125.49(9)°),[28] and considering that the six-coordinate ionic radii of Dy(III) (0.912 Å) and Tm(III) (0.88 Å) are quite similar,[40] we anticipated a similar N–Dy–N angle for **1-Dy**. However, previous computational studies on a series of model two-coordinate DyL_2 compounds (L = mono- or di-anionic monodentate C- or N-donor ligand) predicted that U_{eff} should decrease regularly with bending (e.g. $[Dy\{N(SiH_3)_2\}_2]$; U_{eff} = 2072 cm^{-1} at 180° N–Dy–N, and 919 cm^{-1} at 120°),[27] thus **1-Dy** remained a desirable synthetic target.

The N–Dy–N angle in **1-Dy** (128.7(2)°) is far more bent than the corresponding $Cp_{centroid}\cdots Dy\cdots Cp_{centroid}$ angle of any isolated dysprosocenium cation (smallest known, $[C_5{}^iPr_4H)_2]^+$ = 147.2(8)°),[13] and **1-Dy** has shorter Dy–N bonds (2.206(7) Å mean) than the mean $Dy\cdots Cp_{centroid}$ distances in these systems (e.g. $[C_5{}^iPr_4H)_2]^+$ = 2.29(1) Å).[13] Despite substantially different structures, comparison of the total calculated CF splitting of the $^6H_{15/2}$ multiplet between **1-Dy** and $[Dy(Cp^{ttt})_2]^+$ (for which we have commensurate CASSCF-SO calculations; Cp^{ttt} = $\{C_5H_2{}^tBu_3$-1,2,4$\}$, mean $Dy\cdots Cp_{centroid}$ = 2.416(2) Å and $Cp_{centroid}\cdots Dy\cdots Cp_{centroid}$ = 152.56(7)°)[12] shows that **1-Dy** has a substantially larger splitting (2459 K *vs.* 2124 K); however, the energy gap to the first excited state is slightly smaller (616 *vs.* 703 K), thus it is not

clear-cut which of the two complexes have the largest magnetic anisotropy. The static electronic structures of these cations are clearly insufficient to solely dictate their SMM qualities, as U_{eff} for **1-Dy** (924(17) K) is roughly half the value observed for $[Dy(Cp^{ttt})_2]^+$ (1780(40) K).[43] Conventional usage of the average transition matrix elements of magnetic moment to infer magnetic relaxation probabilities[27] suggests that the U_{eff} value for **1-Dy** should be near the top of the CF manifold (Figure S99), whilst the experimentally-determined U_{eff} value lies in between the first and second excited state. This discrepancy highlights that the static electronic structure alone is insufficient to predict relaxation dynamics. While this would be an excellent opportunity to deploy our recent methods to calculate magnetic relaxation dynamics *ab initio*,[55,56] unfortunately for **1-Dy** there are eight formula units in the crystallographic unit cell (1472 atoms), thus this system is currently too large to perform periodic DFT calculations. We propose that the modulation of the CF by phonons (i.e. spin-phonon coupling) has a larger impact on the electronic states in **1-Dy** than for $[Dy(Cp^R)_2]^+$, because in the former complex the CF is almost exclusively dominated by two flexible monoatomic donor ligands rather than the more rigid η^5-Cp^R rings in $[Dy(Cp^R)_2]^+$ and related derivatives,[12-22] which have been shown to be crucial for dictating spin dynamics in $[Dy(Cp^{ttt})_2]^+$.[57]

Conclusions

In this work, the isolation of compounds containing the $[Dy\{N(Si^iPr)_3\}_2]^+$ cation has realized a long-standing goal to synthesize a formally two-coordinate Dy(III) complex, allowing the magnetic properties of this new class of SMM to be determined. We have found a larger than predicted effect of the N–Dy–N angle on SMM behavior, with the significantly bent geometry of $[Dy\{N(Si^iPr)_3\}_2]^+$ resulting in relatively low-lying and highly mixed excited m_J states. Frozen solution magnetic data indicate a species with substantially slower relaxation dynamics, suggesting that a more linear N–Dy–N angle can be adopted in this phase, but this could not be unambiguously confirmed. We propose that fast magnetic relaxation in $[Dy\{N(Si^iPr)_3\}_2]^+$ arises from a combination of its large deviation from linearity and the flexible coordination environment, in accord with the rigidity of coordinated ligands being of equal importance to the control of molecular geometry for SMMs to show high blocking temperatures.

Experimental Section

Experimental materials and methods.

All manipulations were conducted under argon with the strict exclusion of oxygen and water by using Schlenk line and glove box techniques. Glassware was flame-dried under vacuum prior to use. Argon was passed through a column of activated 3 Å molecular sieves and Cu catalyst prior to use. C_6H_6 and C_6D_6 were purchased anhydrous, degassed, and stored under argon over a K mirror or activated 3 Å molecular sieves, respectively. *n*-Hexane was refluxed over molten K for 3 days, distilled, and stored under argon over a K mirror. C_6H_5F and 1,2-$C_6H_5F_2$ were stirred over neutral alumina for 4-6 h, filtered, refluxed over CaH_2 for 3 days, distilled, and stored under argon over activated 3 Å molecular sieves. Hexamethyldisiloxane (HMDSO) was refluxed over CaH_2 for 3 days, distilled, and stored under argon over activated 3 Å molecular sieves. $[Ln(BH_4)_3(THF)_3]$ (Ln = Y, Dy),[34] $[HNEt_3][Al\{OC(CF_3)_3\}_4]$,[17] and $[CPh_3][Al\{OC(CF_3)_3\}_4]$[35] were prepared according to literature procedures; $[K\{N(Si^iPr_3)_2\}]$ was prepared by an adapted literature procedure,[24] which is detailed in the Supporting Information.

NMR spectra (see Figures S1–S48) of **1-Ln**, **2-Ln**, **3-Ln**, **4-Ln**, **5-Y**/$HN(Si^iPr_3)_2$, $HN(Si^iPr_3)_2$ and $[K\{N(Si^iPr_3)_2\}]$ were recorded at 298 K on a Bruker AVIII HD 400 cryoprobe spectrometer operating at 400.07 (^{1}H) 128.36 (^{11}B), 100.60 (^{13}C), 376.40 (^{19}F) or 79.48 (^{29}Si) MHz. Chemical shifts are reported in ppm and coupling constants in Hz. ^{1}H and $^{13}C\{^1H\}$ DEPTQ NMR spectra recorded in C_6D_6 are referenced to the residual solvent signal.[58] Spectra recorded in proteosolvents were locked to, and where possible referenced with, an internal sealed capillary of C_6D_6. The solution magnetic susceptibilities of **1-Dy**, **2-Dy**, **3-Dy** and **4-Dy** were determined at 298 K by the Evans method;[36] ^{1}H NMR spectra recorded in C_6H_5F or 1,2-$C_6H_4F_2$ were referenced using the highest intensity peak of the highest frequency fluoroarene multiplet (δ_H: 6.87 or 6.85 respectively). $^{11}B/^{11}B\{^1H\}$ (H_3BO_3/D_2O), ^{19}F ($C_7H_5F_3/CDCl_3$) and $^{29}Si\{^1H\}$ DEPT90 ($SiMe_4$) NMR spectra were referenced to external standards. The $C(CF_3)_3$ carbon resonances of the $[Al\{OC(CF_3)_3\}_4]^-$ anion were not observed in the $^{13}C\{^1H\}$ NMR spectra of **1-Ln**, likely due to quadrupolar

broadening by the 100% abundant $I = 5/2$ ^{27}Al nuclei and coupling to multiple 100% abundant $I = 1/2$ ^{19}F nuclei.

ATR-IR spectra of **1-Ln**, **2-Ln**, **3-Ln** and **4-Ln** were recorded as microcrystalline powders using a Bruker Alpha FT-IR spectrometer with a Platinum-ATR module within a nitrogen-filled glovebox at ambient temperature (See Figures S49–S56). Elemental analysis (C, H, N) samples were prepared in an argon-filled glovebox and the analysis carried out either by Mr. Martin Jennings and Mrs. Anne Davies at the Microanalytical service, Department of Chemistry, the University of Manchester, or the Elemental Analysis Services Team, Science Centre, London Metropolitan University. Elemental analysis values obtained for **1-Ln**, **2-Ln**, **3-Ln** and **4-Ln** typically gave carbon compositions that were lower than expected values; this was attributed to carbide formation, which we have observed reproducibly for Ln {N(Si^{i}Pr$_3$)$_2$} complexes.[24,25,28,29]

Single crystal XRD data were collected on either an Oxford Diffraction Agilent Supernova diffractometer equipped with a CCD area detector and a mirror-monochromated Mo Kα source (**1-Y**, **2-Dy**, **3-Dy**, **3-Dy·0.5KBH$_4$·1,2-C$_6$H$_4$F$_2$**, **4-Y**), a Rigaku XtalLAB Synergy-S diffractometer equipped with a HyPix 6000HE photon counting pixel array detector with a mirror-monochromated Mo Kα X-ray source (**4-Dy**), or a Rigaku FR-X diffractometer equipped with a HyPix 6000HE photon counting pixel array detector and a mirror-monochromated X-ray source (**1-Dy**, **2-Y**, **3-Y**, **3-Y·0.5KBH$_4$·C$_6$H$_6$**) (λ = 0.71073 Å for Mo Kα or λ = 1.5418 Å for Cu Kα radiation, Figures S61–S70 and Tables S1–S3). Intensities were integrated from data recorded on 0.5° (**1-Dy**, **2-Y**, **3-Y**, **3-Y·0.5KBH$_4$·C$_6$H$_6$**), or 1° (**1-Y**, **2-Dy**, **3-Dy**, **3-Dy·0.5KBH$_4$·1,2-C$_6$H$_4$F$_2$**, **4-Dy**, **4-Y**) frames by ω rotation. Cell parameters were refined from the observed positions of all strong reflections in each data set. A Gaussian grid face-indexed with a beam profile was applied for all structures.[59] The structures were solved using SHELXT;[60] the datasets were refined by full-matrix least-squares on all unique F^2 values.[60] Anisotropic displacement parameters were used for all non-hydrogen atoms with constrained riding hydrogen geometries, with the exception of borohydride H atoms, which were located in the difference map and refined isotropically; U_{iso}(H) was set at 1.2 (1.5 for methyl groups) times U_{eq} of the parent atom. The largest features in final difference syntheses

were close to heavy atoms and were of no chemical significance. CrysAlisPro[59] was used for control and integration, and SHELX[60,61] was employed through OLEX2[62] for structure solution and refinement. ORTEP-3,[63] and POV-Ray[64] were used for molecular graphics.

Powder XRD data of a microcrystalline sample of **1-Dy** mounted with a minimum amount of fomblin were collected at 100(2) K using a Rigaku FR-X rotating anode single crystal X-ray diffractometer using Cu Kα radiation (λ = 1.5418 Å) with a Hypix-6000HE detector and an Oxford Cryosystems nitrogen flow gas system (Figure S71). Data were collected between 2–70 °θ with a detector distance of 150 mm and a beam divergence of 1.5 mRad using CrysAlisPro.[59] For data processing, the instrument was calibrated using silver behenate as standard, then the data were reduced and integrated using CrysAlisPro.[59] Le Bail profile analysis was performed using JANA2006 software.[65]

Magnetic measurements of **1-Dy** (Figures S72–S98 and Tables S5–S9) were performed on a Quantum Design MPMS3 superconducting quantum interference device (SQUID) magnetometer at The University of Manchester or either a MPMS XL magnetometer or PPMS Evercool II susceptometer housed at the Centre de Recherche Paul Pascal at temperatures between 1.8 and 300 K and dc magnetic fields ranging from –7 to +7 T (MPMS3 and MPMS3 XL) or –9 to +9 T (PPMS Evercool II). The MPMS3 measurements were collected on a finely ground powder sample of **1-Dy** (27.4 mg) restrained in eicosane (22.0 mg) and a 200 mM fluorobenzene (0.102 g) solution of **1-Dy** (35.7 mg), prepared in a glovebox under an atmosphere of argon. The borosilicate tubes were flame-sealed under vacuum and loaded into a plastic straw held in place by friction between diamagnetic tape at the top of the tube and the straw. The solution sample was flash-frozen in liquid nitrogen and rapidly cooled in zero field after loading into the instrument. Measurements were performed in dc scan mode using 40 mm scan length and 6 s scan time. Equilibrium susceptibility measurements were performed on cooling in temperature settle mode 1.8–300 K (solid) or 1.8–180 K (frozen solution) in 0.1 T dc field. Field dependence (*H*) of the magnetization (*M*) curves (2 K, 0–7 T) and *M vs. H* hysteresis curves (± 5 T for 2–7 K, ± 3 T for 8–10 or 12 K) were performed in continuous sweep mode with a sweep rate of 22 Oe s^{-1}. Raw magnetic data were scaled for the shape of the sample using a Quantum Design MPMS3 Geometry Correction Simulator (correction factor 1.003 for solid, 0.817

for solution), corrected for the diamagnetic contribution of the sample holder (straw + borosilicate tube), and corrected for the mass of eicosane using calibrated blanks or for the mass of fluorobenzene using Pascal's constants.[66] The magnetic susceptibility was corrected for the intrinsic diamagnetism of the sample estimated as the molecular weight (g mol^{-1}) multiplied by -0.5×10^{-6} cm^3 K mol^{-1}. Ac magnetic data were recorded for the frozen solution of **1-Dy** at 0.1–1000 Hz between 2–76 K. Low temperature ac data (2–13 K) were fit to the Havriliak-Negami model and high temperature (31–79 K) data were fit to the double generalized Debye model in CC-FIT2 5.0.1.[43-45]

The MPMS XL and PPMS Evercool II measurements were collected on polycrystalline samples of **1-Dy** in sealed polypropylene (PP) bags; for the PPMS VSM DC measurements the sample was suspended in mineral oil (MPMS RSO dc: 40.2 mg **1-Dy**, 10.9 mg PP; PPMS VSM dc: 19.5 mg **1-Dy**, 18.3 mg PP, 13.9 mg oil; MPMS ac and PPMS ACMS ac: 40.2 mg **1-Dy**, 10.9 mg PP; MPMS ac: 22.9 mg **1-Dy**, 9.46 mg PP) in a glovebox under an atmosphere of argon; data were collected *via*: (i) a MPMS XL for dc measurements using the RSO option with fields up to 7 T, and for ac measurements in the 0.001–1500 Hz range; and, (ii) a PPMS Evercool II for dc measurements with the large bore VSM option with fields up to 9 T and for the ac measurements with the ACMS-II option in the 10–10000 Hz range. The FC/ZFC measurements were performed from 50 K cooling to 1.85 K without dc field (reset magnet). The field (10 Oe) was set at 1.85 K and ZFC measurements were recorded upon heating up to 50 K. FC cooling measurements were performed by cooling from 50 to 1.85 K, and FC heating data were collected upon heating from 1.85 to 50 K. During the MPMS XL and PPMS Evercool II experiments, it was clear the amplitude of the magnetization for **1-Dy** decreased slightly over a period of several weeks, and more rapidly during sample transfer/loading in the experimental setup; we attribute this to a small amount of sample decomposition as **1-Dy** is relatively air- and moisture-sensitive. However, no modification of the global, qualitative magnetic behavior was seen, with no shift or shape modification of the relaxation process. Therefore, the amplitude of the magnetic data presented herein were normalized to the MPMS3 measurements collected at Manchester directly after the synthesis and isolation of **1-Dy**. We attribute the systematically lower intensity of magnetization and susceptibility data measured in Bordeaux to minor

decomposition of the sample during shipping. The maximum normalization factor used in this study was 1.19, which also incorporates errors in the sample mass, magnetometer calibration, and background corrections. Ac data for solid **1-Dy** were fitted with the generalized Debye model with MagSuite software, restraining the frequency window to where the model fits well.[67]

Computational methods.

OpenMolcas[50] was used to perform CASSCF-SO calculations on **1-Dy** to determine its electronic structure (Figures S99 and S100 and Table S10). The molecular geometry from the single crystal XRD structure was used with no optimization, taking the largest disorder component only. Integrals were performed in the SEWAD module using basis sets from ANO-RCC library[68–71] with VTZP quality for Dy atoms, VDZP quality for the N atoms, and VDZ quality for all remaining atoms, employing the second-order DKH transformation. Cholesky decomposition of the two-electron integrals with a threshold of 10^{-8} was performed to save disk space and reduce computational demand. The molecular orbitals (MOs) were optimized in state-averaged CASSCF calculations in the RASSCF module, where the active space was defined by the nine 4f electrons in the seven 4f orbitals of Dy(III). Three such calculations were performed independently for each possible spin state, where 21 roots were included for S = 5/2, 224 roots were included for S = 3/2, and 490 roots were included for S = 1/2. The wavefunctions obtained from these CASSCF calculations were then mixed by spin orbit coupling in the RASSI module, where all 21 S = 5/2 states, 128 of the S = 3/2 states, and 130 of the S = 1/2 states were included. SINGLE_ANISO was used to decompose the resulting spin-orbit wave functions into the CF Hamiltonian formalism.[72] Diamond was employed for molecular graphics.[73]

DFT geometry optimizations and vibrational analyses were performed on the cation of **1-Y**, **2-Y**, the monomer of **3-Y**, and **4-Y**, for the purposes of assigning experimental IR spectra (Figures S57–S60). All calculations were executed by the Orca 5.0 software package at the PBE0[74,75]-D4[76,77] / def2-TZVP[78] level (including the default effective core potential for yttrium[79]). The default Orca 5.0 integration grids, convergence method, and convergence thresholds (for both SCF and geometry iterations) where used

throughout. The SCF energy calculations were expedited through employ of the RIJCOSX approximation[80] (and associated def2/J auxiliary basis set[81]) and DIIS convergence acceleration[82] (as is default in Orca 5.0). Geometry-optimized structures were verified as being minima on the potential energy surface through the absence of imaginary vibrational modes. A linear energy scaling was applied to the computed IR spectra.

Synthesis.

[Y{N(Si^{i}Pr$_3$)$_2$}$_2$][Al{OC(CF$_3$)$_3$}$_4$] (1-Y). C_6H_5F (5 mL) was added to a mixture of **4-Y** (0.168 g, 0.221 mmol) and $[CPh_3][Al\{OC(CF_3)_3\}_4]$ (0.242 g, 0.200 mmol) and the reaction mixture was stirred for 18 h at 20 °C. The resulting suspension was filtered and layered with excess *n*-hexane (*ca*. 20 mL), which upon slow diffusion afforded the title compound as colorless needles. The crystals were isolated and dried thoroughly *in vacuo*. Yield: 0.251 g, 0.146 mmol, 73%. Anal. Calcd for $C_{52}H_{84}AlF_{36}O_4N_2Si_4Y$ (1713.42 g mol^{-1}) C, 36.45; H, 4.94, N, 1.63. Found: C, 34.38; H, 4.51, N, 1.41. ^{1}H NMR (400.07 MHz, C_6H_5F): δ 1.15 (d, $^3J_{HH}$ = 7.4 Hz, 72H, C*H*$_3$), 0.86 (hept, $^3J_{HH}$ = 7.4 Hz, 12H, C*H*). ^{13}C{^{1}H} DEPTQ NMR (100.60 MHz, C_6H_5F): δ 123.28 (q, $^1J_{FC}$ = 294 Hz, CF_3), 19.57 (s, *C*H$_3$), 18.25 (s, *C*H). ^{19}F NMR (376.40 MHz, C_6H_5F): δ –75.05 (s, C*F*$_3$). ^{29}Si{^{1}H} DEPT90 NMR (79.48 MHz, C_6H_5F): δ –4.79 (s, *Si*^{i}Pr$_3$). FTIR (ATR, microcrystalline): $\tilde{\nu}$ = 2945 (m), 2867 (m), 1465 (m), 1352 (m), 1296 (m), 1274 (m), 1241 (m), 1208 (s) 1167 (m), 968 (s), 953 (m), 920 (m), 880 (m), 725 (s) cm^{-1}.

[Dy{N(Si^{i}Pr$_3$)$_2$}$_2$][Al{OC(CF$_3$)$_3$}$_4$] (1-Dy). C_6H_5F (5 mL) was added to a mixture of **4-Dy** (0.350 g, 0.418 mmol) and $[CPh_3][Al\{OC(CF_3)_3\}_4]$ (0.484 g, 0.400 mmol) and the reaction mixture was stirred for 18 h at 20 °C. The resulting suspension was filtered and layered with excess *n*-hexane (*ca*. 20 mL), which upon slow diffusion afforded the title compound as colorless needles. The crystals were isolated and dried thoroughly *in vacuo*. Yield: 0.567 g, 0.317 mmol, 79%. Anal. Calcd for $C_{52}H_{84}AlDyF_{36}O_4N_2Si_4$ (1786.91 g mol^{-1}) C, 34.95; H, 4.74, N, 1.57. Found: C, 33.66; H, 4.37, N, 1.41. χT product = 14.2 cm^3 mol^{-1} K, μ_{eff} = 10.7 μ_B mol^{-1} (Evans method). ^{1}H NMR (400.07 MHz, C_6D_6): δ 4.76 (br, fwhm ≈ 60 Hz), 4.23 (br, fwhm ≈ 50 Hz), 3.95 (br, fwhm ≈ 160 Hz), 3.67 (br, fwhm ≈ 60 Hz). ^{19}F NMR (376.40 MHz, C_6H_5F): δ 97.22

(br, fwhm ≈ 280 Hz, CF_3). FTIR (ATR, microcrystalline): $\tilde{\nu}$ = 2945 (m), 2867 (m), 1465 (m), 1352 (m), 1296 (m), 1274 (m), 1241 (m), 1208 (s) 1167 (m), 968 (s), 953 (m), 920 (m), 880 (m), 725 (s) cm^{-1}.

[Y{N(Si^{i}Pr$_3$)$_2$}(BH$_4$)$_2$(THF)] (2-Y). C_6H_5F (10 mL) was added to a mixture of [Y(BH$_4$)$_3$(THF)$_3$] (2.389 g, 5.000 mmol) and [K{N(Si^{i}Pr$_3$)$_2$}] (1.857 g, 5.050 mmol) and the resulting suspension was stirred at 20 °C for 1 h. The volatiles were removed *in vacuo* and the residues extracted into *n*-hexane (3 × 20 mL) with vigorous agitation and filtered. The solution was concentrated to *ca*. 10 mL and stored at –25 °C, affording the title complex as colorless needles, which were isolated and thoroughly dried *in vacuo*. Yield: 2.298 g, 4.424 mmol, 88%. Anal. Calcd for $C_{22}H_{58}B_2ONSi_2Y$ (519.35 g mol^{-1}) C, 50.87; H, 11.26, N, 2.70. Found: C, 49.55; H, 11.09, N, 2.45. ^{1}H NMR (400.07 MHz, C_6D_6, 298 K): δ 3.60 (br s, fwhm ≈ 19 Hz, 4H, CH$_2$C*H*$_2$O), 1.33 (d, $^3J_{HH}$ = 7.3 Hz, 36H, C*H*$_3$CH), 1.26 (q, 8H, $^1J_{BH}$ = 81 Hz, B*H*$_4$), 1.15 (sept, $^3J_{HH}$ = 7.3 Hz, 6H, CH$_3$C*H*), 1.06 (br s, fwhm ≈ 21 Hz, 4H, C*H*$_2$CH$_2$O). ^{11}B NMR (128.36 MHz, C_6D_6, 298 K): δ 22.0 (p, $^1J_{BH}$ = 81 Hz, *B*H$_4$). ^{13}C{^{1}H} DEPTQ NMR (100.60 MHz, C_6D_6, 298 K): δ 74.6 (CH$_2$*C*H$_2$O), 24.8 (*C*H$_2$CH$_2$O), 20.6 (*C*H$_3$CH), 18.4 (CH$_3$*C*H). ^{29}Si{^{1}H} DEPT90 NMR (79.48 MHz, C_6D_6, 298 K): δ –2.7 (*Si*^{i}Pr$_3$). FTIR (ATR, microcrystalline): $\tilde{\nu}$ = 2951 (m), 2867 (m), 2488 (m), 2178 (b), 1463 (m), 1185 (m), 1095 (w), 999 (m), 923 (s), 873 (s), 719 (s), 653 (s) cm^{-1}.

[Dy{N(Si^{i}Pr$_3$)$_2$}(BH$_4$)$_2$(THF)] (2-Dy). C_6H_5F (10 mL) was added to a mixture of [Dy(BH$_4$)$_3$(THF)$_3$] (2.757 g, 5.000 mmol) and [K{N(Si^{i}Pr$_3$)$_2$}] (1.857 g, 5.050 mmol) and the resulting suspension was stirred at 20 °C for 1 h. The volatiles were removed *in vacuo* and the residues extracted into *n*-hexane (3 × 20 mL) with vigorous agitation and filtered. The solution was concentrated to *ca*. 10 mL and stored at –25 °C, affording the title complex as pale-yellow needles, which were isolated and thoroughly dried *in vacuo*. Yield: 2.470 g, 4.165 mmol, 83%. Anal. Calcd for $C_{22}H_{58}B_2DyONSi_2$ (592.94 g mol^{-1}) C, 44.56; H, 9.86, N, 2.36. Found: C, 43.86; H, 10.22, N, 2.84. χT product = 13.9 cm^3 mol^{-1} K, μ_{eff} = 10.5 μ_B mol^{-1} (Evans method). ^{1}H NMR (400.07 MHz, C_6D_6): δ 40.13 (vbr, fwhm ≈ 650 Hz, OC*H*$_2$CH$_2$), 1.55 (br, fwhm ≈ 20 Hz), 1.11 (br, fwhm ≈ 20 Hz, C*H*$_3$), 0.78 (br, fwhm ≈ 20 Hz), 0.63 (br, fwhm ≈ 20 Hz), –42.80 (vbr, fwhm

≈ 1610 Hz, OCH_2CH_2). The BH_4 resonance was not located. $^{11}B\{^1H\}$ NMR (128.36 MHz, C_6D_6): δ –18.14 (vbr, fwhm ≈ 2490 Hz), BH_4. FTIR (ATR, microcrystalline): $\tilde{\nu}$ = 2951 (m), 2867 (m), 2488 (m), 2178 (b), 1463 (m), 1185 (m), 1095 (w), 999 (m), 923 (s), 873 (s), 719 (s), 653 (s) cm^{-1}.

[Y{N(Si^{i}Pr$_3$)$_2$}(BH$_4$)(μ-BH$_4$)]$_4$ (3-Y). In a long re-sealable ampule, **2-Y** (4.290 g, 8.259 mmol) was heated to 120 °C in the solid state at *ca.* 0.01 mbar for 2 h, resulting in the partial sublimation of the solid material. After cooling to ambient temperature, the residues were found to have a mass of 3.699 g (8.270 mmol assuming the formula weight of **3-Y**), consistent with the removal of 99.2% of the bound THF. The ^1H, ^{11}B, ^{13}C and ^{29}Si NMR spectra of this amorphous material were found to be identical to an authentic crystalline sample of **3-Y**, prepared as follows. In a long re-sealable ampule, **2-Y** (1.390 g, 2.676 mmol) was heated to 150 °C in the solid state at *ca.* 0.01 mbar for 2 h, resulting in the partial sublimation of the solid material, and minor production of a high-boiling colorless oil. After cooling to ambient temperature, the residues were extracted into 1,2-$C_6H_4F_2$ (3 × 5 mL), filtered, and the solution concentrated to *ca*. 5 mL. Slow diffusion of excess *n*-hexane (*ca.* 20 mL) at –25 °C gave the title complex as colorless plates, which were isolated and thoroughly dried *in vacuo*. An additional crop was obtained upon storage at –25 °C after concentrating the fully diffused supernatant to *ca.* 5 mL. Yield: 0.641 g, 1.433 mmol, 54%. On one occasion, a sample of **3-Y** contaminated with trace KBH_4 was recrystallized by slow evaporation of benzene. Several crystals of **3-Y·0.5KBH$_4$·C$_6$H$_6$** were identified in the crop by single crystal XRD, though as a homogenous sample of the impurity was neither obtained nor sought, no further characterization data are reported. Characterization data for **3-Y**: Anal. calcd for $C_{18}H_{50}B_2NSi_2Y$ (447.25 g mol^{-1}) C, 48.33; H, 11.27, N, 3.13. Found: C, 45.67; H, 10.77, N, 2.81. ^1H NMR (400.07 MHz, C_6D_6): δ 1.13–1.07 (m, 50H, C*H*CH_3, CHC*H*$_3$ and B*H*$_4$). ^{11}B NMR (128.36 MHz, C_6D_6, 298 K): δ –20.7 (br., fwhm ≈ 480 Hz, *B*H_4), –3.6 (br., fwhm ≈ 2240 Hz, μ-*B*H_4). $^{13}C\{^1H\}$ DEPTQ NMR (100.60 MHz, C_6D_6): δ 19.3 (s, *C*H_3CH), 14.9 (s, CH_3*C*H). $^{29}Si\{^1H\}$ DEPT90 NMR (79.48 MHz, C_6D_6): δ –3.7 (s, *Si*^{i}Pr$_3$). ^1H NMR (400.07 MHz, $C_6H_4F_2$, C_6D_6): δ 1.13–1.00 (m, 50H, C*H*CH_3, CHC*H*$_3$ and B*H*$_4$). ^{11}B NMR (128.36 MHz, $C_6H_4F_2$, C_6D_6, 298 K): δ –20.9 (br. p, $^1J_{BH}$ ≈ 80 Hz, fwhm ≈ 120 Hz, *B*H_4). $^{13}C\{^1H\}$ DEPTQ NMR (100.60 MHz, $C_6H_4F_2$, C_6D_6): δ

18.8 (s, *C*H$_3$CH), 14.9 (s, CH$_3$*C*H). ^{29}Si{^{1}H} DEPT90 NMR (79.48 MHz, C$_6$H$_4$F$_2$, C$_6$D$_6$): δ –3.6 (s, *Si*^{i}Pr$_3$). FTIR (ATR, microcrystalline): $\tilde{\nu}$ = 2945 (m), 2865 (m), 2747 (w), 2519 (w), 2291 (m), 2178 (w), 2142 (w), 1467 (m), 1241 (s), 1194 (s), 908 (s), 873 (s), 715 (s), 655 (s) cm^{-1}.

[Dy{N(Si^{i}Pr$_3$)$_2$}(BH$_4$)(μ-BH$_4$)]$_4$ (3-Dy). In a long re-sealable ampule, **2-Dy** (0.3822 g, 0.6446 mmol) was heated to 120 °C in the solid state at *ca.* 0.01 mbar for 2 h, resulting in the partial sublimation of the solid material. After cooling to ambient temperature, the residues were found to have a mass of 0.3357 g (0.6446 mmol assuming the formula weight of **3-Dy**), consistent with the removal of 100% of the bound THF. The ^{1}H and ^{11}B NMR spectra of this amorphous material were found to be identical to an authentic crystalline sample of **3-Dy**, prepared as follows. In a long re-sealable ampule, **2-Dy** (1.770 g, 2.985 mmol) was heated to 150 °C in the solid state at *ca.* 0.01 mbar for 2 h, resulting in the partial sublimation of the solid material, and minor production of a high-boiling colorless oil. After cooling to ambient temperature, in a glovebox the residues were returned to the base of the flask and the above procedure repeated. After cooling to ambient temperature, the residues were extracted into 1,2-C$_6$H$_4$F$_2$ (3 × 5 mL), filtered, and the solution concentrated to *ca*. 5 mL. Slow diffusion of excess *n*-hexane (*ca.* 20 mL) at –25 °C afforded the title complex as pale yellow plates, which were isolated and thoroughly dried *in vacuo*. An additional crop of the title complex was obtained upon storage at –25 °C after concentrating the fully diffused supernatant to *ca.* 5 mL. Yield: 1.067 g, 2.049 mmol, 67%. As described for **3-Y**, trace KBH$_4$ contamination led to the formation of several crystals of **3-Dy·0.5KBH$_4$·C$_6$H$_4$F$_2$-1,2** following recrystallization from 1,2-C$_6$H$_4$F$_2$ layered with hexane. This complex was characterized by single crystal XRD only. Characterization data for **3-Dy**: Anal. Calcd for C$_{18}$H$_{50}$B$_2$DyNSi$_2$ (520.84 g mol^{-1}) C, 41.50; H, 9.67, N, 2.69. Found: C, 39.55; H, 9.81, N, 2.55. χT product = 12.5 cm^3 mol^{-1} K, μ_{eff} = 10.0 μ_B mol^{-1} (Evans method). ^{1}H NMR (400.07 MHz, C$_6$D$_6$): δ 1.71 (br, fwhm ≈ 20 Hz, C*H*$_3$), 1.25 (br, fwhm ≈ 30 Hz), 0.34 (br, fwhm ≈ 30 Hz). ^{11}B{^{1}H} NMR (128.36 MHz, C$_6$D$_6$): δ –9.94 (vbr, fwhm ≈ 2450 Hz, B*H*$_4$). FTIR (ATR, microcrystalline): $\tilde{\nu}$ = 2947 (m), 2867 (m), 2751 (w), 2517 (w), 2287 (m), 2166 (w), 2143 (w), 1467 (m), 1208 (s), 1189 (s), 904 (s), 873 (s), 715 (s), 656 (s) cm^{-1}.

[Y{N(Si^{i}Pr$_3$)$_2$}$_2$(BH$_4$)] (4-Y). A solution of **3-Y** (0.447 g, 1.000 mmol) and [K{N(Si^{i}Pr$_3$)$_2$}] (0.734 g, 2.000 mmol) in benzene (10 mL) was stirred at 30 °C for 72 h. The volatiles were then removed *in vacuo* and the residues extracted into *n*-hexane and filtered. The volatiles were again removed *in vacuo*, and [HNEt$_3$][Al{OC(CF$_3$)$_3$}$_4$] (0.535 g, 0.500 mmol) followed by benzene (10 mL) added. The resulting suspension was vigorously stirred for 4 h at 20 °C, after which the volatiles were removed *in vacuo* and the residues extracted into HMDSO (3 × 1 mL) and filtered. Storage of the solution at –35 °C afforded the title compound as colorless blocks, which were isolated and thoroughly dried *in vacuo*. Yield: 0.178 g, 0.234 mmol, 23% with respect to **3-Y**. Anal. Calcd for $C_{36}H_{88}BN_2Si_4Y$ (761.08 g mol^{-1}) C, 56.81; H, 11.65, N, 3.68. Found: C, 51.98; H, 11.17; N, 2.12. ^{1}H NMR (400.07 MHz, C_6D_6): δ 1.47 (qd, $^1J_{BH}$ = 72 Hz, $^1J_{YH}$ = 14 Hz, 4H, B*H*$_4$), 1.35 (d, $^3J_{HH}$ = 7.4 Hz, 72H, C*H*$_3$), 1.06 (hept, $^3J_{HH}$ = 7.5 Hz, 12H, C*H*). ^{11}B NMR (128.36 MHz, C_6D_6): δ -21.41 (p, $^1J_{BH}$ = 86 Hz, *B*H$_4$). ^{13}C{^{1}H} DEPTQ NMR (100.60 MHz, C_6D_6): δ 21.0 (s, *C*H$_3$CH), 19.8 (s, CH$_3$*C*H). ^{29}Si{^{1}H} DEPT90 NMR (79.48 MHz, C_6D_6): δ –3.36 (s, *Si*^{i}Pr$_3$). FTIR (ATR, microcrystalline): $\tilde{\nu}$ = 2943 (s), 2864 (s), 2756 (w), 2731 (w), 2495 (w), 2229 (br), 1463 (m), 1241 (s), 1216 (s), 941 (s), 879 (s), 698 (s), 658 (s) cm^{-1}.

[Dy{N(Si^{i}Pr$_3$)$_2$}$_2$(BH$_4$)] (4-Dy). A solution of **3-Dy** (0.520 g, 1.000 mmol) and [K{N(Si^{i}Pr$_3$)$_2$}] (0.734 g, 2.000 mmol) in benzene (10 mL) was stirred at 30 °C for 72 h. The volatiles were then removed *in vacuo* and the residues extracted into *n*-hexane and filtered. The volatiles were again removed *in vacuo*, and [HNEt$_3$][Al{OC(CF$_3$)$_3$}$_4$] (0.535 g, 0.500 mmol) followed by benzene (10 mL) added. The resulting suspension was vigorously stirred for 4 h at 20 °C, after which the volatiles were removed *in vacuo* and the residues extracted into HMDSO (3 × 1 mL) and filtered. Storage of the solution at –35 °C afforded the title compound as colorless blocks, which were isolated and thoroughly dried *in vacuo*. Yield: 0.089 g, 0.117 mmol, 12% with respect to **3-Dy**. Anal. Calcd for $C_{36}H_{88}BDyN_2Si_4$ (834.67 g mol^{-1}) C, 51.80; H, 10.63, N, 3.36. Found: C, 49.16; H, 10.73; N, 2.97. χT product = 12.6 cm^3 mol^{-1} K, μ_{eff} = 10.1 μ_B mol^{-1} (Evans method). ^{1}H NMR (400.07 MHz, C_6D_6): δ 1.35 (br, fwhm ≈ 25 Hz), 0.62 (br, fwhm ≈ 18 Hz). ^{11}B{^{1}H}

NMR (128.36 MHz, C_6D_6): δ –14.1 (vbr, fwhm ≈ 1690 Hz, BH_4). FTIR (ATR, microcrystalline): $\tilde{\nu}$ = 2943 (s), 2864 (s), 2753 (w), 2727 (w), 2488 (w), 2240 (br), 1463 (m), 1239 (s), 1212 (s), 939 (s), 879 (s), 698 (s), 659 (s) cm^{-1}.

[Y{N(Si^{i}Pr$_3$)$_2$}{N(Si^{i}Pr$_3$)[Si(^{i}Pr)$_2${CH(Me)CH$_2$}]-κ^2-N,C}] (5-Y). The HMDSO-insoluble residues (250 mg) from a synthesis of **3-Y** similar to that outlined above, and found by ^{1}H NMR spectroscopy to contain 11.3 mol% **1-Y** (42.4 mg, 0.0247 mmol) and 88.7 mol% [HNEt$_3$][Al{OC(CF$_3$)$_3$}$_4$] (207.6 mg, 0.194 mmol), were combined with [K{N(Si^{i}Pr$_3$)$_2$}] (150 mg, 0.408 mmol) and the mixture suspended in benzene (5 mL). After stirring at ambient temperature for 1 h, the volatiles were removed *in vacuo* and the residues extracted into hexane. The volatiles were again removed *in vacuo*, and a portion of the resulting colorless oil containing a mixture of the title compound and HN(Si^{i}Pr$_3$)$_2$ was analyzed in C_6D_6 solution by NMR spectroscopy. ^{1}H NMR (400.07 MHz, C_6D_6): 1.67 (d, $^3J_{HH}$ = 6.2 Hz, 3H, Si^{i}Pr$_2$CH(C*H*$_3$)CH$_2$Y), 1.45 (d, $^3J_{HH}$ = 6.9 Hz, 3H, Si^i*Pr*$_2$CH(CH$_3$)CH$_2$Y), 1.43 (d, $^3J_{HH}$ = 6.5 Hz, 3H, Si^i*Pr*$_2$CH(CH$_3$)CH$_2$Y), 1.38–1.32 (m, 9H, C*H*$_3$), 1.30–1.25 (m, 54H, C*H*$_3$), 1.12 – 1.02 (obsc. m, 9H, C*H*), 1.00–0.90 (m, 3H, C*H*). ^{13}C{^{1}H} DEPTQ NMR (100.60 MHz, C_6D_6, selected signals): δ 55.34 (d, $^1J_{YC}$ = 47.4 Hz, Si^{i}Pr$_2$CH(CH$_3$)*C*H$_2$Y), 24.50 (s, Si^{i}Pr$_2$CH(*C*H$_3$)CH$_2$Y, 21.79 (s, Si^i*Pr*$_2$CH(CH$_3$)CH$_2$Y), 20.69 (s, Si^i*Pr*$_2$CH(CH$_3$)CH$_2$Y). ^{29}Si{^{1}H} DEPT90 NMR (79.48 MHz, C_6D_6): δ, –3.32 (s, ^{i}Pr$_3$*Si*NSi^{i}Pr$_2$CH(CH$_3$)CH$_2$), –5.75 (s, ^{i}Pr$_3$*Si*N*Si*^{i}Pr$_3$), –7.62 (s, ^{i}Pr$_3$SiN*Si*^{i}Pr$_2$CH(CH$_3$)CH$_2$).

Associated Content

Author contributions

J.E.-K. and D.P.M. provided the original synthetic concept. J.E.-K. synthesized and characterized the compounds. J.E.-K. collected, solved, and refined the single crystal XRD datasets, whilst I.J.V.-Y. collected, solved, and refined the powder XRD dataset; G.F.S.W. performed additional refinement of both single crystal and powder XRD data and finalized the single crystal XRD data. M.R., G.K.G. and R.C. collected magnetic data. M.R., G.K.G., R.C. and N.F.C. interpreted and fitted magnetic data. J.E.-K.

performed DFT calculations to assign IR spectra. G.K.G. performed the CASSCF-SO calculations. R.C. and N.F.C. supervised the magnetism component, N.F.C. supervised the computational component, D.P.M. supervised the synthetic component, and both N.F.C. and D.P.M. directed the research. J.E.-K., G.K.G., N.F.C. and D.P.M. wrote the manuscript, with contributions from all authors.

Supporting Information

Additional experimental details, materials, methods, and data associated with this manuscript are compiled in the Supporting Information.

Additional Information

Research data files supporting this publication are available from FigShare at https://figshare.com/doi/10.6084/m9.figshare.23807376.

Accession Codes

CCDC 2284722–2284732 contain the supplementary crystallographic data for this paper. These data can be obtained free of charge via www.ccdc.cam.ac.uk/data_request/cif, or by emailing data_request@ccdc.cam.ac.uk, or by contacting The Cambridge Crystallographic Data Centre, 12 Union Road, Cambridge, CB2 1EZ, UK; fax: +44 1223 336033.

Notes

The authors declare no competing financial interests.

Acknowledgements

We thank the University of Manchester for access to the Computational Shared Facility, and the European Research Council (StG-851504 and CoG-816268) and the UK EPSRC (EP/R002605X/1, EP/P001386/1, EP/S033181/1 and EP/T011289/1) for funding. We acknowledge the EPSRC UK National

Electron Paramagnetic Resonance Service for access to the SQUID magnetometer and the National Nuclear User Facility at the Center for Radiochemical Research for access to a diffractometer. R.C. and M.R. thank the University of Bordeaux, the CNRS, the Region Nouvelle Aquitaine, and Quantum Matter Bordeaux. N.F.C. thanks the Royal Society for a University Research Fellowship (URF191320).

References

(1) Giansiracusa, M. J.; Gransbury, G. K.; Chilton, N. F.; Mills, D. P. Single-Molecule Magnets. In *Encyclopedia of Inorganic and Bioinorganic Chemistry*; Ed. R. A. Scott, John Wiley: Chichester, 2021, DOI:10.1002/9781119951438.eibc2784.

(2) Chilton, N. F. Molecular Magnetism. *Annu. Rev. Mater. Res.* **2022**, *52*, 79–101. https://doi.org/10.1146/annurev-matsci-081420.

(3) Gatteschi, D.; Sessoli, R.; Villain, J. *Molecular Nanomagnets*; Oxford University Press: Oxford, 2006. https://doi.org/10.1093/acprof:oso/9780198567530.001.0001.

(4) Ishikawa, N.; Sugita, M.; Ishikawa, T.; Koshihara, S. Y.; Kaizu, Y. Lanthanide Double-Decker Complexes Functioning as Magnets at the Single-Molecular Level. *J. Am. Chem. Soc.* **2003**, *125* (29), 8694–8695. https://doi.org/10.1021/ja029629n.

(5) Layfield, R. A.; Murugesu, M. *Lanthanides and Actinides in Molecular Magnetism*; Wiley: Hoboken, 2015. DOI: 10.1002/9783527673476.

(6) Liddle, S. T.; Van Slageren, J. Improving f-Element Single Molecule Magnets. *Chem. Soc. Rev.* **2015**, *44* (19), 6655–6669. https://doi.org/10.1039/c5cs00222b.

(7) Liu, J.-L.; Chen, Y.-C.; Tong, M.-L. Symmetry Strategies for High Performance Lanthanide-Based Single-Molecule Magnets. *Chem. Soc. Rev.* **2018**, *47* (7), 2431–2453. https://doi.org/10.1039/c7cs00266a.

(8) Rinehart, J. D.; Long, J. R. Exploiting Single-Ion Anisotropy in the Design of f-Element Single-Molecule Magnets. *Chem. Sci.* **2011**, *2* (11), 2078–2085. https://doi.org/10.1039/c1sc00513h.

(9) Ungur, L.; Chibotaru, L. F. Magnetic Anisotropy in the Excited States of Low Symmetry Lanthanide Complexes. *Phys. Chem. Chem. Phys.* **2011**, *13* (45), 20086–20090. https://doi.org/10.1039/c1cp22689d.

(10) Ungur, L.; Chibotaru, L. F. Strategies toward High-Temperature Lanthanide-Based Single-Molecule Magnets. *Inorg. Chem.* **2016**, *55* (20), 10043–10056. https://doi.org/10.1021/acs.inorgchem.6b01353.

(11) Parmar, V. S.; Mills, D. P.; Winpenny, R. E. P. Mononuclear Dysprosium Alkoxide and Aryloxide Single-Molecule Magnets. *Chem. Eur. J.* **2021**, *27* (28), 7625–7645. https://doi.org/10.1002/chem.202100085.

(12) Goodwin, C. A. P.; Ortu, F.; Reta, D.; Chilton, N. F.; Mills, D. P. Molecular Magnetic Hysteresis at 60 Kelvin in Dysprosocenium. *Nature* **2017**, *548* (7668), 439–442. https://doi.org/10.1038/nature23447.

(13) Randall McClain, K.; Gould, C. A.; Chakarawet, K.; Teat, S. J.; Groshens, T. J.; Long, J. R.; Harvey, B. G. High-Temperature Magnetic Blocking and Magneto-Structural Correlations in a Series of Dysprosium(III) Metallocenium Single-Molecule Magnets. *Chem. Sci.* **2018**, *9* (45), 8492–8503. https://doi.org/10.1039/c8sc03907k.

(14) Guo, F. S.; Day, B. M.; Chen, Y. C.; Tong, M. L.; Mansikkamäki, A.; Layfield, R. A. Magnetic Hysteresis up to 80 Kelvin in a Dysprosium Metallocene Single-Molecule Magnet. *Science* **2018**, *362* (6421), 1400–1403. https://doi.org/10.1126/science.aav0652.

(15) Guo, F.-S.; Day, B. M.; Chen, Y.-C.; Tong, M.-L.; Mansikkamäki, A.; Layfield, R. A. A Dysprosium Metallocene Single-Molecule Magnet Functioning at the Axial Limit. *Angew. Chem. Int. Ed.* **2017**, *56* (38), 11445–11449. https://doi.org/10.1002/anie.201705426.

(16) Guo, F.-S.; Day, B. M.; Chen, Y.-C.; Tong, M.-L.; Mansikkamäki, A.; Layfield, R. A. Corrigendum: A Dysprosium Metallocene Single-Molecule Magnet Functioning at the Axial Limit. *Angew. Chem. Int. Ed.* **2020**, *59* (43), 18844–18844. https://doi.org/10.1002/anie.202010617.

(17) Evans, P.; Reta, D.; Whitehead, G. F. S.; Chilton, N. F.; Mills, D. P. Bis-Monophospholyl Dysprosium Cation Showing Magnetic Hysteresis at 48 K. *J. Am. Chem. Soc.* **2019**, *141* (50), 19935–19940. https://doi.org/10.1021/jacs.9b11515.

(18) Gould, C. A.; McClain, K. R.; Yu, J. M.; Groshens, T. J.; Furche, F.; Harvey, B. G.; Long, J. R. Synthesis and Magnetism of Neutral, Linear Metallocene Complexes of Terbium(II) and Dysprosium(II). *J. Am. Chem. Soc.* **2019**, *141* (33), 12967–12973. https://doi.org/10.1021/jacs.9b05816.

(19) Gould, C. A.; McClain, K. R.; Reta, D.; Kragskow, J. G. C.; Marchiori, D. A.; Lachman, E.; Choi, E.-S.; Analytis, J. G.; Britt, R. D.; Chilton, N. F.; Harvey, B. G.; Long, J. R. Ultrahard Magnetism from Mixed-Valence Dilanthanide Complexes with Metal-Metal Bonding. *Science* **2022**, *375* (6577), 198–202. https://doi.org/10.1126/science.abl5470.

(20) Guo, F. S.; He, M.; Huang, G. Z.; Giblin, S. R.; Billington, D.; Heinemann, F. W.; Tong, M. L.; Mansikkamäki, A.; Layfield, R. A. Discovery of a Dysprosium Metallocene Single-Molecule Magnet with Two High-Temperature Orbach Processes. *Inorg. Chem.* **2022**, *61* (16), 6017–6025. https://doi.org/10.1021/acs.inorgchem.1c03980.

(21) Vanjak, J. C.; Wilkins, B. O.; Vieru, V.; Bhuvanesh, N. S.; Reibenspies, J. H.; Martin, C. D.; Chibotaru, L. F.; Nippe, M. A High-Performance Single-Molecule Magnet Utilizing Dianionic Aminoborolide Ligands. *J. Am. Chem. Soc.* **2022**, *144* (39), 17743–17747. https://doi.org/10.1021/jacs.2c06698.

(22) Vincent, A. H.; Whyatt, Y. L.; Chilton, N. F.; Long, J. R. Strong Axiality in a Dysprosium(III) Bis(Borolide) Complex Leads to Magnetic Blocking at 65 K. *J. Am. Chem. Soc.* **2023**, *145* (3), 1572–1579. https://doi.org/10.1021/jacs.2c08568.

(23) Reta, D.; Kragskow, J. G. C.; Chilton, N. F. Ab Initio Prediction of High-Temperature Magnetic Relaxation Rates in Single-Molecule Magnets. *J. Am. Chem. Soc.* **2021**, *143* (15), 5943–5950. https://doi.org/10.1021/jacs.1c01410.

(24) Chilton, N. F.; Goodwin, C. A. P.; Mills, D. P.; Winpenny, R. E. P. The First Near-Linear Bis(Amide) f-Block Complex: A Blueprint for a High Temperature Single Molecule Magnet. *Chem. Commun.* **2015**, *51*, 101–103. https://doi.org/10.1039/C4CC08312A.

(25) Goodwin, C. A. P.; Chilton, N. F.; Vettese, G. F.; Moreno Pineda, E.; Crowe, I. F.; Ziller, J. W.; Winpenny, R. E. P.; Evans, W. J.; Mills, D. P. Physicochemical Properties of Near-Linear Lanthanide(II) Bis(Silylamide) Complexes (Ln = Sm, Eu, Tm, Yb). *Inorg. Chem.* **2016**, *55* (20), 10057–10067. https://doi.org/10.1021/acs.inorgchem.6b00808.

(26) Blagg, R. J.; Ungur, L.; Tuna, F.; Speak, J.; Comar, P.; Collison, D.; Wernsdorfer, W.; McInnes, E. J. L.; Chibotaru, L. F.; Winpenny, R. E. P. Magnetic Relaxation Pathways in Lanthanide Single-Molecule Magnets. *Nat. Chem.* **2013**, *5* (8), 673–678. https://doi.org/10.1038/nchem.1707.

(27) Chilton, N. F. Design Criteria for High-Temperature Single-Molecule Magnets. *Inorg. Chem.* **2015**, *54* (5), 2097–2099. https://doi.org/10.1021/acs.inorgchem.5b00089.

(28) Nicholas, H. M.; Vonci, M.; Goodwin, C. A. P.; Loo, S. W.; Murphy, S. R.; Cassim, D.; Winpenny, R. E. P.; McInnes, E. J. L.; Chilton, N. F.; Mills, D. P. Electronic Structures of Bent Lanthanide(III) Complexes with Two N-Donor Ligands. *Chem. Sci.* **2019**, *10* (45), 10493–10502. https://doi.org/10.1039/C9SC03431E.

(29) Goodwin, C. A. P.; Réant, B. L. L.; Kragskow, J. G. C.; DiMucci, I. M.; Lancaster, K. M.; Mills, D. P.; Sproules, S. Heteroleptic Samarium(III) Halide Complexes Probed by Fluorescence-Detected L 3-Edge X-Ray Absorption Spectroscopy. *Dalton Trans.* **2018**, *47* (31), 10613–10625. https://doi.org/10.1039/c8dt01452c.

(30) Errulat, D.; Harriman, K. L. M.; Gálico, D. A.; Kitos, A. A.; Mansikkamäki, A.; Murugesu, M. A Trivalent 4f Complex with Two Bis-Silylamide Ligands Displaying Slow Magnetic Relaxation. *Nat. Chem.* **2023**. https://doi.org/10.1038/s41557-023-01208-y.

(31) *The Rare Earth Elements: Fundamentals and Applications*, Atwood, D. A. Ed., John Wiley & Sons Ltd: Chichester, 2012.

(32) Ortu, F.; Mills, D. P. Low-Coordinate Rare-Earth and Actinide Complexes. In *Handbook on the Physics and Chemistry of Rare Earths*, Bünzli, J.-C. G.; Pecharsky, V. K. Eds., Elsevier B. V.: Amsterdam, 2019, Vol. 55, pp 1–87. https://doi.org/10.1016/bs.hpcre.2019.05.001.

(33) Yang, K.; Sun, R.; Zhao, J.; Deng, C.; Wang, B.; Gao, S.; Huang, W. A Combined Synthetic, Magnetic, and Theoretical Study on Enhancing Ligand-Field Axiality for Dy(III) Single-Molecule Magnets Supported by Ferrocene Diamide Ligands. *Inorg. Chem.* **2023**, *62* (25), 9892–9903. https://doi.org/10.1021/acs.inorgchem.3c00896.

(34) Goodwin, C. A. P.; Reta, D.; Ortu, F.; Liu, J.; Chilton, N. F.; Mills, D. P. Terbocenium: Completing a Heavy Lanthanide Metallocenium Cation Family with an Alternative Anion Abstraction Strategy. *Chem. Commun.* **2018**, *54* (66), 9182–9185. https://doi.org/10.1039/c8cc05261a.

(35) Krossing, I.; Brands, H.; Feuerhake, R.; Koenig, S. New Reagents to Introduce Weakly Coordinating Anions of Type $Al(ORF)_4^-$: Synthesis, Structure and Characterization of Cs and Trityl Salts. *J. Fluor. Chem.* **2001**, *112*, 83–90. https://doi.org/10.1016/S0022-1139(01)00490-0.

(36) Sur, S. K. Measurement of Magnetic Susceptibility and Magnetic Moment of Paramagnetic Molecules in Solution by High-Field Fourier Transform NMR Spectroscopy. *J. Magn. Reson.* **1989**, *82*, 169–173. https://www.sciencedirect.com/science/article/pii/0022236489901789.

(37) Kahn, O. *Molecular Magnetism*, VCH-Verlag: Weinheim, 1993.

(38) Niemeyer, M. Reactions of Hypersilyl Potassium with Rare-Earth Metal Bis(Trimethylsilylamides): Addition versus Peripheral Deprotonation. *Inorg. Chem.* **2006**, *45* (22), 9085–9095. https://doi.org/10.1021/ic0613659.

(39) Marks, T. J.; Kolb, J. R. Covalent Transition Metal, Lanthanide, and Actinide Tetrahydroborate Complexes. *Chem. Rev.* **1977**, *77* (2), 263–293. https://doi.org/10.1021/cr60306a004.

(40) Shannon, R. D. Revised Effective Ionic Radii and Systematic Studies of Interatomic Distances in Halides and Chalcogenides. *Acta Crystallogr., Sect. A* **1976**, *32* (5), 751–767. https://doi.org/10.1107/S0567739476001551.

(41) van Vleck, J. H. Paramagnetic Relaxation Times for Titanium and Chrome Alum. *Phys. Rev.* **1940**, *57* (5), 426–447. https://doi.org/10.1103/PhysRev.57.426.

(42) Shrivastava, K. N. Theory of Spin–Lattice Relaxation. *Phys. Stat. Sol. (b)* **1983**, *117* (2), 437–458. https://doi.org/10.1002/pssb.2221170202.

(43) Reta, D.; Chilton, N. F. Uncertainty Estimates for Magnetic Relaxation Times and Magnetic Relaxation Parameters. *Phys. Chem. Chem. Phys.* **2019**, *21* (42), 23567–23575. https://doi.org/10.1039/c9cp04301b.

(44) Blackmore, W. J. A.; Gransbury, G. K.; Evans, P.; Kragskow, J. G. C.; Mills, D. P.; Chilton, N. F. Characterisation of Magnetic Relaxation on Extremely Long Timescales. *Phys. Chem. Chem. Phys.* **2023**, *25*, 16735–16744. https://doi.org/10.1039/D3CP01278F.

(45) https://gitlab.com/chilton-group/cc-fit2.

(46) Ding, Y. S.; Blackmore, W. J. A.; Zhai, Y. Q.; Giansiracusa, M. J.; Reta, D.; Vitorica-Yrezabal, I.; Winpenny, R. E. P.; Chilton, N. F.; Zheng, Y. Z. Studies of the Temperature Dependence of the Structure and Magnetism of a Hexagonal-Bipyramidal Dysprosium(III) Single-Molecule Magnet. *Inorg. Chem.* **2022**, *61* (1), 227–235. https://doi.org/10.1021/acs.inorgchem.1c02779.

(47) Ding, Y. S.; Yu, K. X.; Reta, D.; Ortu, F.; Winpenny, R. E. P.; Zheng, Y. Z.; Chilton, N. F. Field- and Temperature-Dependent Quantum Tunnelling of the Magnetisation in a Large Barrier Single-Molecule Magnet. *Nat. Commun.* **2018**, *9*, 3134. https://doi.org/10.1038/s41467-018-05587-6.

(48) Chiesa, A.; Cugini, F.; Hussain, R.; MacAluso, E.; Allodi, G.; Garlatti, E.; Giansiracusa, M.; Goodwin, C. A. P.; Ortu, F.; Reta, D.; Skelton, J. M.; Guidi, T.; Santini, P.; Solzi, M.; De Renzi, R.; Mills, D. P.; Chilton, N. F.; Carretta, S. Understanding Magnetic Relaxation in Single-Ion Magnets with High Blocking Temperature. *Phys. Rev. B* **2020**, *101*, 174402. https://doi.org/10.1103/PhysRevB.101.174402.

(49) Abragam, A.; Bleaney, B. *Electron Paramagnetic Resonance of Transition Ions*, Oxford University Press: Oxford, 1970.

(50) Orbach, R. Spin-lattice relaxation in rare-earth salts. *Proc. R. Soc. London, Ser. A.* **1961**, *264* (1319), 458–484. https://doi.org/10.1098/rspa.1961.0211.

(51) Topping, C. V.; Blundell, S. J. A.C. Susceptibility as a Probe of Low-Frequency Magnetic Dynamics. *J. Phys. Condens. Matter* **2019**, *31* (1), 013001. https://doi.org/10.1088/1361-648X/aaed96.

(52) Fdez. Galván, I.; Vacher, M.; Alavi, A.; Angeli, C.; Aquilante, F.; Autschbach, J.; Bao, J. J.; Bokarev, S. I.; Bogdanov, N. A.; Carlson, R. K.; Chibotaru, L. F.; Creutzberg, J.; Dattani, N.; Delcey, M. G.; Dong, S. S.; Dreuw, A.; Freitag, L.; Frutos, L. M.; Gagliardi, L.; Gendron, F.; Giussani, A.; González, L.; Grell, G.; Guo, M.; Hoyer, C. E.; Johansson, M.; Keller, S.; Knecht, S.; Kovačević, G.; Källman, E.; Li Manni, G.; Lundberg, M.; Ma, Y.; Mai, S.; Malhado, J. P.; Malmqvist, P. Å.; Marquetand, P.; Mewes, S. A.; Norell, J.; Olivucci, M.; Oppel, M.; Phung, Q. M.; Pierloot, K.; Plasser, F.; Reiher, M.; Sand, A. M.; Schapiro, I.; Sharma, P.; Stein, C. J.; Sørensen, L. K.; Truhlar, D. G.; Ugandi, M.; Ungur, L.; Valentini, A.; Vancoillie, S.; Veryazov, V.; Weser, O.; Wesołowski, T. A.; Widmark, P. O.; Wouters, S.; Zech, A.; Zobel, J. P.; Lindh, R. OpenMolcas: From Source Code to Insight. *J. Chem. Theor. Comput.* **2019**, *15* (11), 5925–5964. https://doi.org/10.1021/acs.jctc.9b00532.

(53) *Functional Molecular Silicon Compounds II*; Scheschkewitz, D. Ed. Structure and Bonding; Springer International Publishing: Cham, 2014; Vol. 156. https://doi.org/10.1007/978-3-319-03734-9.

(54) Goodwin, C. A. P.; Mills, D. P. Silylamides: Towards a Half-Century of Stabilising Remarkable f-Element Chemistry. In *Specialist Periodical Reports: Organometallic Chemistry*, Fairlamb, I. J. S.; Lynam, J.; Patmore, N. J.; Elliott, P. Eds. RSC Publishing: Cambridge, 2017, Vol. 41, pp. 123–156. https://doi.org/10.1039/9781782626923-00123.

(55) Kragskow, J. G. C.; Mattioni, A.; Staab, J. K.; Reta, D.; Skelton, J. M.; Chilton, N. F. Spin–Phonon Coupling and Magnetic Relaxation in Single-Molecule Magnets. *Chem. Soc. Rev.* **2023**, *52*, 4567–4585. https://doi.org/10.1039/D2CS00705C.

(56) Nabi, R.; Staab, J. K.; Mattioni, A.; Kragskow, J. G. C.; Reta, D.; Skelton, J. M.; Chilton, N. F. Accurate and Efficient Spin-Phonon Coupling and Spin Dynamics Calculations for Molecular Solids. *ChemRxiv* **2023**, DOI: 10.26434/chemrxiv-2023-6q06z-v2.

(57) Ortu, F.; Reta, D.; Ding, Y. S.; Goodwin, C. A. P.; Gregson, M. P.; McInnes, E. J. L.; Winpenny, R. E. P.; Zheng, Y. Z.; Liddle, S. T.; Mills, D. P.; Chilton, N. F. Studies of Hysteresis and Quantum Tunnelling of the Magnetisation in Dysprosium(III) Single Molecule Magnets. *Dalton Trans.* **2019**, *48* (24), 8541–8545. https://doi.org/10.1039/c9dt01655d.

(58) Fulmer, G. R.; Miller, A. J. M.; Sherden, N. H.; Gottlieb, H. E.; Nudelman, A.; Stoltz, B. M.; Bercaw, J. E.; Goldberg, K. I. NMR Chemical Shifts of Trace Impurities: Common Laboratory Solvents, Organics, and Gases in Deuterated Solvents Relevant to the Organometallic Chemist. *Organometallics* **2010**, *29* (9), 2176–2179. https://doi.org/10.1021/om100106e.

(59) *CrysAlis PRO*, Agilent Technologies Ltd. Yarnton, England, 2014.

(60) Sheldrick, G. M. SHELXT - Integrated Space-Group and Crystal-Structure Determination. *Acta Crystallogr., Sect. A* **2015**, *71*, 3–8. https://doi.org/10.1107/S2053273314026370.

(61) Sheldrick, G. M. Crystal Structure Refinement with SHELXL. *Acta Crystallogr., Sect. C* **2015**, *71*, 3–8. https://doi.org/10.1107/S2053229614024218.

(62) Dolomanov, O. V.; Bourhis, L. J.; Gildea, R. J.; Howard, J. A. K.; Puschmann, H. OLEX2: A Complete Structure Solution, Refinement and Analysis Program. *J. Appl. Cryst.* **2009**, *42* (2), 339–341. https://doi.org/10.1107/S0021889808042726.

(63) Farrugia, L. J. WinGX and ORTEP for Windows: An Update. *J. Appl. Cryst.* **2012**, *45* (4), 849–854. https://doi.org/10.1107/S0021889812029111.

(64) *Persistence of Vision Raytracer*, v.3.7, Persistence of Vision Raytracer Pty. Ltd., 2013. Retrieved from http://www.povray.org/download/.

(65) Kabova, E. A.; Blundell, C. D.; Muryn, C. A.; Whitehead, G. F. S.; Vitorica-Yrezabal, I. J.; Ross, M. J.; Shankland, K. SDPD-SX: Combining a Single Crystal X-Ray Diffraction Setup with Advanced Powder Data Structure Determination for Use in Early Stage Drug Discovery. *CrystEngComm* **2022**, *24*, 4337–4340. https://doi.org/10.1039/d2ce00387b.

(66) Bain, G. A.; Berry, J. F. Diamagnetic Corrections and Pascal's Constants. *J. Chem. Ed.* **2008**, *85* (4), 532. https://doi.org/10.1021/ed085p532.

(67) *MagSuite* v.3.2. Rouzières, M., *Zenodo* 2023. https://doi.org/10.5281/zenodo.7509746.

(68) Roos, B. O.; Veryazov, V.; Widmark, P.-O. Relativistic Atomic Natural Orbital Type Basis Sets for the Alkaline and Alkaline-Earth Atoms Applied to the Ground-State Potentials for the Corresponding Dimers. *Theor. Chem. Acc.* **2004**, *111* (2–6), 345–351. https://doi.org/10.1007/s00214-003-0537-0.

(69) Roos, B. O.; Lindh, R.; Malmqvist, P. Å.; Veryazov, V.; Widmark, P. O. Main Group Atoms and Dimers Studied with a New Relativistic ANO Basis Set. *J. Phys. Chem. A* **2004**, *108* (15), 2851–2858. https://doi.org/10.1021/jp031064+.

(70) Roos, B. O.; Lindh, R.; Malmqvist, P.-Å.; Veryazov, V.; Widmark, P.-O. New Relativistic ANO Basis Sets for Transition Metal Atoms. *J. Phys. Chem. A* **2005**, *109* (29), 6575–6579. https://doi.org/10.1021/jp0581126.

(71) Roos, B. O.; Lindh, R.; Malmqvist, P.-Å.; Veryazov, V.; Widmark, P.-O.; Borin, A. C. New Relativistic Atomic Natural Orbital Basis Sets for Lanthanide Atoms with Applications to the Ce Diatom and LuF 3. *J. Phys. Chem. A* **2008**, *112* (45), 11431–11435. https://doi.org/10.1021/jp803213j.

(72) Chibotaru, L. F.; Ungur, L. Ab Initio Calculation of Anisotropic Magnetic Properties of Complexes. I. Unique Definition of Pseudospin Hamiltonians and Their Derivation. *J. Chem. Phys.* **2012**, *137* (6), 064112. https://doi.org/10.1063/1.4739763.

(73) *Diamond - Crystal and Molecular Structure Visualization*; Crystal Impact v.4.6.8. Putz, H.; Brandenburg, H., Bonn, Germany, 2022.

(74) Adamo, C.; Barone, V. Toward Reliable Density Functional Methods without Adjustable Parameters: The PBE0 Model. *J. Chem. Phys.* **1999**, *110* (13), 6158–6170. https://doi.org/10.1063/1.478522.

(75) Perdew, J. P.; Ernzerhof, M.; Burke, K. Rationale for Mixing Exact Exchange with Density Functional Approximations. *J. Chem. Phys.* **1996**, *105* (22), 9982–9985. https://doi.org/10.1063/1.472933.

(76) Caldeweyher, E.; Bannwarth, C.; Grimme, S. Extension of the D3 Dispersion Coefficient Model. *J. Chem. Phys.* **2017**, *147* (3), 034112. https://doi.org/10.1063/1.4993215.

(77) Caldeweyher, E.; Ehlert, S.; Hansen, A.; Neugebauer, H.; Spicher, S.; Bannwarth, C.; Grimme, S. A Generally Applicable Atomic-Charge Dependent London Dispersion Correction. *J. Chem. Phys.* **2019**, *150* (15), 154122. https://doi.org/10.1063/1.5090222.

(78) Weigend, F.; Ahlrichs, R. Balanced Basis Sets of Split Valence, Triple Zeta Valence and Quadruple Zeta Valence Quality for H to Rn: Design and Assessment of Accuracy. *Phys. Chem. Chem. Phys.* **2005**, *7* (18), 3297–3305. https://doi.org/10.1039/b508541a.

(79) Andrae, D.; Häußermann, U.; Dolg, M.; Stoll, H.; Preuß, H. Energy-Adjusted Ab Initio Pseudopotentials for the Second and Third Row Transition Elements. *Theor. Chim. Acta* **1990**, *77* (2), 123–141. https://doi.org/10.1007/BF01114537.

(80) Neese, F.; Wennmohs, F.; Hansen, A.; Becker, U. Efficient, Approximate and Parallel Hartree–Fock and Hybrid DFT Calculations. A 'Chain-of-Spheres' Algorithm for the Hartree–Fock Exchange. *Chem. Phys.* **2009**, *356* (1–3), 98–109. https://doi.org/10.1016/j.chemphys.2008.10.036.

(81) Weigend, F. Accurate Coulomb-Fitting Basis Sets for H to Rn. *Phys. Chem. Chem. Phys.* **2006**, *8* (9), 1057–1065. https://doi.org/10.1039/b515623h.

(82) Pulay, P. Convergence acceleration of iterative sequences. The case of SCF iteration. *Chem. Phys. Lett.* **1980**, *73* (2), 393–398. https://doi.org/10.1016/0009-2614(80)80396-4.